An Adaptive Virtual Impedance Control Scheme Based on Small-AC-Signal Injection for Unbalanced and Harmonic Power Sharing in Islanded Microgrids

Baojin Liu ⬤ , *Student Member, IEEE*, Zeng Liu, *Member, IEEE*, Jinjun Liu ⬤ , *Fellow, IEEE*,
Ronghui An ⬤ , *Student Member, IEEE*, Haoyang Zheng, and Yidong Shi

Abstract—To address the unbalanced and harmonic power sharing issue among parallel inverters caused by feeder impedance mismatch in islanded microgrids, an adaptive virtual impedance control method is proposed based on the injection of an extra small ac signal (SACS) in the output voltage of each inverter. Similar to the principle of active power–frequency droop, the frequency of the injected signal droops with the output unbalanced and harmonic power, while the active power produced by the injected SACS is detected to adjust the virtual impedance at the fundamental negative sequence and selected harmonic frequencies, which will tune the distribution of unbalanced and harmonic power in the system. When the injected SACSs of each inverter synchronize with each other and reach a common frequency in steady state, the virtual impedance of each inverter will be matched to each other for evenly sharing the unbalanced and harmonic power. This proposed method requires neither communication links among parallel inverters nor feeder impedance information. Furthermore, the control parameter design method based on modeling and stability analysis of the proposed control structure is discussed in detail. Finally, simulation and experimental results are provided to validate the effectiveness of the proposed scheme.

Index Terms—Droop control, nonlinear load, parallel inverters, signal injection, unbalanced load.

I. INTRODUCTION

TRADITIONAL centralized power generation has recently lost its attraction due to increasing concerns about environmental pollution and the fossil energy crisis. Distributed generation (DG) may be a promising alternative as it can facilitate the interconnection of renewable energy sources (RESs), such as photovoltaics, wind turbines, and hydropower [1]. To increase the reliability, flexibility, and intelligence of a DG system, several DG units, together with loads and energy storage systems (ESSs), are integrated into a single controllable entity, known as

a microgrid. Under normal conditions, microgrids are connected to the utility grid to supply or consume electrical power according to the energy management command. However, microgrids should also be capable of disconnecting from the utility grid when faults and contingencies occur, and maintaining operation in islanded mode to feed local load [2].

Usually, RESs are connected to the point of common coupling (PCC) through power electronics-based interfaces such as inverters [3]. Therefore, the coordinative control of parallel inverters plays a critical role in the robust operation of microgrids. During islanded operation, one of the major requirements is to ensure that load power is properly shared by the DG units according to their power ratings to avoid overloading of inverters. To fulfill the power sharing requirement without dependence on communication links among DG units, active power–frequency (P–ω) and reactive power–voltage amplitude (Q–E) droop control, which mimics the characteristics of a synchronous generator, has been proposed and is well accepted [4]–[7]. However, traditional droop control is derived based on analysis of the fundamental voltage model and only takes averaged active and reactive power into account, which is incapable of compensating the unbalanced and harmonic power sharing error caused by feeder impedance mismatch and discrepancy of DG inverters. Moreover, microgrids may be subjected to significant degrees of unbalanced load and nonlinear load conditions with the increase of single-phase load and power electronics-based devices. For example, LED lighting equipment, unsymmetrical short-circuit faults [8], electric vehicle charge stations, variable-speed drives, etc., consume large amounts of unbalanced and harmonic power. Unfortunately, conventional solutions used with passive or active power filters are not suitable for a DG system due to cost concerns and the strongly distributed feature of the load [9]. Therefore, the sharing performance of unbalanced and harmonic power among parallel inverters tends to a more complex but equally important issue with active and reactive power, which will be focused in this paper. Note that, although traditional droop control also displays difficulty in the sharing of reactive power, this issue is addressed in many previous publications [10]–[13], and is beyond the scope of this paper.

Various methods aimed at solving either the unbalanced power or the harmonic power sharing issue in islanded microgrids, or both, have been proposed. These methods can be classified into two categories according to whether or not they

require communication links, i.e., communication-based methods [14]–[22] and communication-less methods [24]–[34]. Among the communication-based methods, the methods in [14]–[17] have been developed based on the microgrid hierarchical control framework so as to compensate the voltage distortion and unbalance at the PCC and at the same time share the compensation effort among DG units. The compensation command is calculated at the secondary or tertiary control level and is sent to the primary level through communication links. Control methods proposed in [18]–[20] are used to enhance power sharing with the help of a microgrid central controller, which is responsible for sending the harmonic voltage component at the PCC or a compensation synchronization flag to DG local controllers. In recent years, more advanced control algorithms such as consensus-based methods [21], [22] have been introduced to enhance power sharing in microgrids. Since the consensus algorithm is located in DG local controllers and only requires communication between neighbor inverters, the robustness of DG system could be much improved. With advances in information technology, various communication approaches have been used in microgrids with no technical difficulties [23]. However, the presence of critical communication infrastructures among DG units or different control levels still increases the risk of communication failure and the cost of construction. Moreover, it also deteriorates the plug-and-play feature in microgrids. Therefore, communication-based methods are not sufficiently reliable or flexible for large DG systems.

Considering that DG units may be geographically distributed far apart in microgrids, communication-less control schemes are preferable. An intuitive way to share the unbalanced and/or harmonic power is to introduce a virtual output impedance that is much larger than the feeder impedance at the fundamental negative sequence and harmonic frequencies [24]–[28]. These methods are easily implemented but come with a tradeoff between power sharing effectiveness and PCC voltage quality. Larger virtual impedance can improve the power sharing performance, but the unbalanced or harmonic voltage drop with the virtual impedance will increase, worsening voltage quality. Instead, smaller virtual impedance avoids the voltage distortion problem, but the power sharing error cannot be effectively compensated. Furthermore, direct droop relationship between unbalanced or harmonic power and virtual impedance (or conductance) has been developed in [29]–[31] and [33]. The essential idea is to adjust the virtual impedance (or conductance) according to the output unbalanced or harmonic power in each DG unit. Therefore, the power sharing performance under intensive unbalanced and nonlinear load conditions is improved and voltage distortion is compensated. However, the power sharing error is inevitable when the feeder impedance differs greatly in a highly distributed system. To eliminate harmonic power sharing error, the concept of negative virtual harmonic impedance and Z_h–H droop is suggested in [32] without affecting voltage quality at the load bus. Unfortunately, the exact value of line impedance is required to design the droop coefficient, which dramatically increases computational burden and implementation difficulty. To avoid requiring the line impedance value, Tuladhar *et al.* [34] proposed to inject a small ac signal (SACS),

whose frequency is controlled by the harmonic power, into the output voltage of each inverter as a control signal. Meanwhile, the active power produced by the SACS is detected to adjust the voltage control loop bandwidth to realized harmonic power sharing. Although SACS injection is a useful technique, variation of the voltage control loop bandwidth may affect the dynamic performance and stability of the inverter. Besides, the stability analysis and parameter design are not given, and the sharing of unbalanced power is not considered either.

To overcome the aforementioned limitations, this paper proposes an adaptive virtual impedance control scheme for unbalanced and harmonic power sharing in islanded microgrids. At beginning, inspired by the method proposed in [34], an extra SACS, whose frequency is determined by a droop relationship with the output unbalanced and harmonic power, is generated in the output voltage of each inverter. Then, the active power produced by the injected signal is detected and utilized to adjust the virtual impedance at terminal of each DG unit. Eventually, the regulation of virtual impedance will tune the distribution of unbalanced and harmonic power directly without affecting system dynamic performance or stability. The features of the proposed adaptive virtual impedance control scheme can be summarized as follows. First, local information is just needed in the control scheme for each inverter; thus, the communication is not required. Second, according to the principle of P–ω droop, the frequency of the injected signal will reach a common value in steady state, ensuring the even sharing of unbalanced and harmonic power, or proportional sharing, according to the power rating, and the aforementioned power sharing issue in [24]–[31] and [33] is overcome. Third, since the virtual impedance is adjusted automatically to make total output impedance of the inverter match with each other, the proposed scheme is independent of the knowledge of feeder impedance, and the issue of feeder impedance in [32] is handled. Finally, since virtual impedance, rather than the voltage control bandwidth, is regulated for sharing both unbalanced and harmonic power, the issues of dynamic and stability associated with variation of voltage loop in [34] are avoided.

Moreover, this paper presents a comprehensive parameter design for the proposed control scheme based on steady-state, transient, and small-signal modeling and analysis of the islanded microgrids. Finally, simulation and experimental results are provided to validate the effectiveness of the proposed method.

The remainder of this paper is structured as follows. Section II briefs the principle of traditional droop control and analyzes the power distribution in an islanded microgrid. Then, the basic idea and details of the proposed control method are introduced comprehensively in Section III. Section IV presents the methodology of parameter design based on modeling and stability analysis. Simulation and experimental results are given in Section V, and conclusions are finally drawn in Section VI.

II. BASIC PRINCIPLE OF DROOP CONTROL AND POWER DISTRIBUTION ANALYSIS

A typical structure of islanded microgrids studied in this paper is shown in Fig. 1. In each DG unit, the RESs or ESSs are
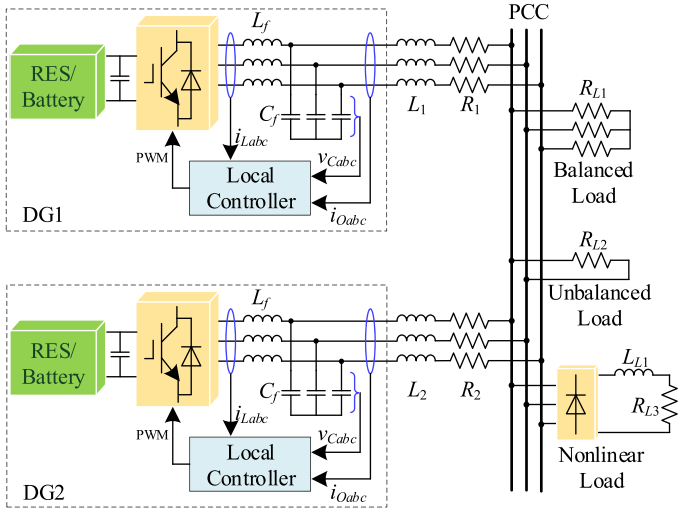
Fig. 1. Structure of the studied islanded microgrid consisting of two DG units, balanced load, unbalanced load, and nonlinear load.

connected to the PCC through three-phase voltage source inverters, and an inductance and capacitance (*LC*) filter is employed to filter out switching frequency noise. The feeder impedance may differ greatly due to the random distribution of DG units, where the feeder inductance and resistance are represented by L_1, L_2, and R_1, R_2, respectively. A generalized load condition, including balanced load, unbalanced load, and nonlinear load, is considered. Note that the topology studied is a three-phase three-wire system. Therefore, zero-sequence current is not considered in this paper. To aid understanding of the proposed method, the principle of traditional droop control and the definition of electric power are reviewed in this section. Afterward, the distribution of unbalanced and harmonic power under traditional droop control is analyzed.

A. Basic Principle of Droop Control

To realize the power sharing and to synchronize each inverter, the traditional P–ω and Q–E droop method is adopted as shown in Fig. 2. The droop characteristics can be mathematically expressed as follows:

$$\omega^* = \omega_0 - k_p(P - P_0) \tag{1}$$

$$E^* = E_0 - k_q(Q - Q_0) \tag{2}$$

where ω^* and ω_0 are the reference and nominal angular frequencies, respectively; E^* and E_0 are the reference and nominal voltage magnitudes, respectively; P_0 and Q_0 are, respectively, the dispatched active and reactive power at the frequency ω_0 and voltage amplitude E_0; k_p and k_q are the droop coefficients, which are positive values; and P and Q are the measured output active and reactive power, respectively. To eliminate the ripples in P and Q, a low-pass filter (LPF) with relatively low cutoff frequency is usually included in the power calculation process.

Based on the frequency and amplitude references obtained in (1) and (2), the fundamental voltage reference for the voltage

regulation in $\alpha\beta$ stationary reference frame can be derived as

$$v_{1\alpha}^* = E^* \cos\left(\int \omega^* \, dt\right) \tag{3a}$$

$$v_{1\beta}^* = E^* \sin\left(\int \omega^* \, dt\right) \tag{3b}$$

where $v_{1\alpha}^*$ and $v_{1\beta}^*$ represent the α-axis and β-axis components of the fundamental voltage reference, respectively. Then, the voltage regulator adjusts the output voltage to follow this reference value by using a proportional resonant (PR) controller whose resonance frequency is adaptively tuned according to (1) [19].

An inverter under droop control can be modeled as a controlled voltage source, whose frequency and amplitude are regulated according to the output active and reactive power. Fig. 3 shows the equivalent circuit of the studied islanded microgrid at the fundamental positive sequence. The output active and reactive power of DG*i* (*i* denotes 1 or 2) can be derived as in (4) and (5) under inductive feeder impedance conditions [5], [6].

$$P_i = \frac{E_i U_L \sin \delta_i}{X_i} \tag{4}$$

$$Q_i = \frac{E_i (E_i - U_L \cos \delta_i)}{X_i} \tag{5}$$

where X_i is the reactance of the feeder inductor and δ_i is the phase angle difference between terminal voltage E_i and PCC voltage U_L. Usually, δ_i is assumed to be very small, and by substituting $\sin \delta_i \approx \delta_i$ and $\cos \delta_i \approx 1$, (4) and (5) can be simplified as

$$P_i = \frac{E_i U_L \delta_i}{X_i} \tag{6}$$

$$Q_i = \frac{E_i (E_i - U_L)}{X_i}. \tag{7}$$

Based on (6) and (7), we can conclude that P increases with phase angle difference and Q increases with voltage amplitude.

To improve understanding of the proposed unbalanced and harmonic power sharing method in Section III, the basic operating principle of P–ω droop is explained here. Assuming that P_1 is larger than P_2 due to disturbance, then the frequency of DG1 will be lower than that of DG2 according to (1), leading to a reduction of δ_1 and an increase of δ_2. Then, the output active power P_1 will decrease and P_2 will increase based on (6). This forms a self-regulating feedback mechanism to share the active power. Eventually, all of the DG units synchronize with one another and reach a common frequency. Therefore, the P–ω droop control can always achieve active power sharing even with feeder impedance mismatch and discrepancy of DG inverters.

It should be noted that, if the DG units have the same power rating, then the droop coefficients should be designed identically to achieve equal power sharing. Nevertheless, when units of different power ratings are connected in parallel, the droop coefficients should be designed according to the following relationships [5]:

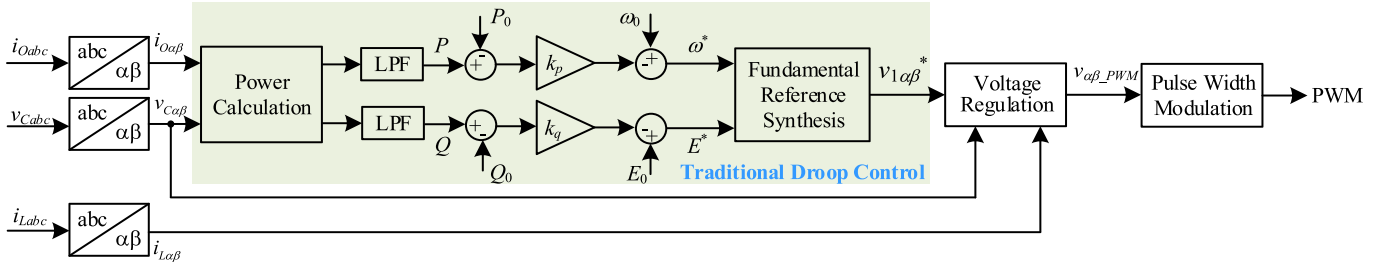$$k_{p1}S_1 = k_{p2}S_2 = \cdots = k_{pn}S_n \tag{8}$$

Fig. 2. Control block diagram of DG with the traditional P–ω and Q–E droop method.
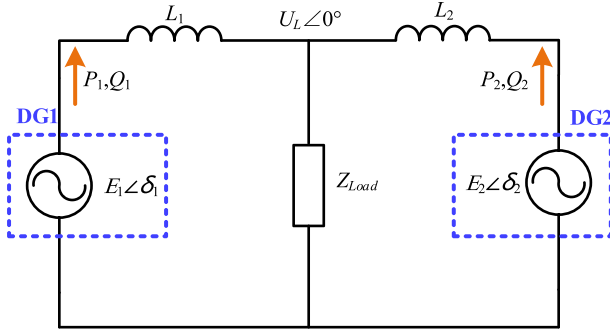

Fig. 3. Equivalent circuit of the studied islanded microgrid presenting the fundamental positive sequence components.

$$k_{q1}S_1 = k_{q2}S_2 = \cdots = k_{qn}S_n \qquad (9)$$

where S_i is the power rating of inverter i. In this way, the load power can be shared in the same proportions as for the ratings of the inverters.

According to the aforementioned analysis, two features of traditional droop control can be observed. First, the control variables are fundamental frequency ω and amplitude E. Second, the LPF for power calculation determines that only fundamental powers are considered. Therefore, the traditional droop control method is derived based on the fundamental voltage model, and does not consider the fundamental negative sequence and harmonic frequencies. This is the essential reason why traditional droop control is incapable of sharing unbalanced and harmonic power.

B. Definition of Unbalanced and Harmonic Power

Since the unbalanced and harmonic power may not be as familiar as P and Q to the readers, some basic points regarding definitions of electric power are briefly reviewed, according to IEEE standard 1459 [35]. For a three-phase power system under unbalanced and nonsinusoidal conditions, the resolution of effective apparent power S_e can be expressed as

$$S_e = \sqrt{S_{e1}^2 + S_{eN}^2} \qquad (10)$$

where S_{e1} and S_{eN} represent the fundamental and nonfundamental effective apparent power, respectively. S_{e1} can be further

expanded as

$$
\begin{aligned}
S_{e1} &= 3V_{e1}I_{e1} \\
&= 3\sqrt{\left(V_1^+\right)^2 + \left(V_1^-\right)^2}\sqrt{\left(I_1^+\right)^2 + \left(I_1^-\right)^2} \\
&= 3\sqrt{\left(V_1^+I_1^+\right)^2 + \left(V_1^+I_1^-\right)^2 + \left(V_1^-I_1^+\right)^2 + \left(V_1^-I_1^-\right)^2}
\end{aligned}
$$
$$(11)$$

where V_{e1} and I_{e1} are the fundamental rms voltage and current, respectively; V_1^+ and V_1^- are the fundamental positive and negative sequence voltages, respectively; and I_1^+ and I_1^- are the fundamental positive and negative sequence currents, respectively. Aside from the fundamental positive sequence apparent power $(V_1^+I_1^+)$, the remaining three terms constitute the unbalanced power. Note that the negative sequence voltage in a practical power system is strictly limited to a small range [36], so terms related to negative sequence voltage ($V_1^-I_1^+$ and $V_1^-I_1^-$) can be ignored. Therefore, the definition of unbalanced power (denoted by Q_U) can be expressed as

$$Q_U \approx 3V_1^+I_1^-. \qquad (12)$$

Similarly, S_{eN} can be further expressed as

$$S_{eN} = 3\sqrt{\left(V_{e1}I_{eH}\right)^2 + \left(V_{eH}I_{e1}\right)^2 + \left(V_{eH}I_{eH}\right)^2} \qquad (13)$$

where V_{eH} and I_{eH} represent harmonic rms voltage and current, respectively. The voltage distortion is also strictly limited in a practical power system, so the power terms related to V_{eH} can be neglected. Therefore, the definition of harmonic power (denoted by Q_H) can be expressed as

$$Q_H \approx 3V_1^+I_{eH}. \qquad (14)$$

Based on the aforementioned analysis, Q_U and Q_H are essentially the product of fundamental voltage and negative sequence or harmonic current, respectively, and their physical meaning is to evaluate the amount of var caused by load unbalance or nonlinearity. To simplify the analysis and discussion, Q_U and Q_H are combined together and defined as unbalanced and harmonic power (denoted by Q_{UH} hereafter). The expression for Q_{UH} is as follows:

$$
\begin{aligned}
Q_{UH} &= \sqrt{Q_U^2 + Q_H^2} \\
&= 3V_1^+\sqrt{\left(I_1^-\right)^2 + \left(I_{eH}\right)^2}.
\end{aligned}
$$
$$(15)$$

Note that the fundamental positive sequence voltage between each DG unit is very close, because the droop coefficient k_q is
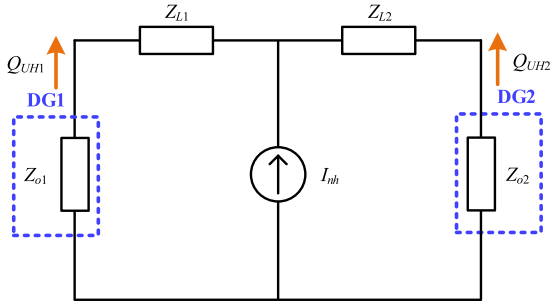
Fig. 4. Equivalent circuit of the studied islanded microgrid presenting the fundamental negative sequence and harmonic frequency components.

designed to be very small. Therefore, we can replace V_1^+ with the nominal voltage to simplify the calculation of Q_{UH}, as shown in (16). Under this condition, the essence of unbalanced and harmonic power sharing is to share the fundamental negative sequence and harmonic current. Moreover, only the dominant low-order harmonic current needs to be selected according to load characteristic to avoid overcurrent. In this paper, the -1st, -5th, 7th, and -11th current components are adopted, with the minus symbol indicating negative sequence.

$$Q_{UH} = \frac{3}{\sqrt{2}} E_0 \sqrt{\left(I_1^-\right)^2 + \left(I_{eH}\right)^2}. \qquad (16)$$

C. Power Distribution Analysis

As mentioned earlier, all of the DG units under droop control operate in the voltage-controlled mode. Hence, they should be modeled as controlled voltage sources at the fundamental positive sequence as shown in Fig. 3. The reference voltage generated by the droop equations determines the inverter output voltage and ensures sharing of the fundamental active and reactive power. Note that the reference voltage is purely sinusoidal and three-phase balanced with the fundamental frequency. Therefore, the inverter should be regarded as a short circuit with a small output impedance at the fundamental negative sequence and harmonic frequencies, as depicted in Fig. 4 [19], [32], [33]. The unbalanced and nonlinear load is modeled as current source I_{nh}, which injects the fundamental negative sequence and harmonic current into the system. Z_{o1} and Z_{o2} are inverter output impedance, and Z_{L1} and Z_{L2} represent the feeder impedance. According to Fig. 4, the negative sequence and harmonic current are distributed based on the equivalent impedance (i.e., sum of Z_o and Z_L) on each branch. Note that the load impedance at the PCC is much larger than the equivalent impedance, so it is not considered when analyzing the distribution of I_{nh}.

To simplify the discussion, two assumptions are made in this paper. First, the inverter output impedance Z_o is assumed to be much smaller than the feeder impedance. Therefore, it can hardly affect the power distribution. For example, the output impedance for a well-designed DG inverter is usually below -30 dB (about $0.03\ \Omega$) at low-frequency range to suppress the distortion in output voltage when feeding nonlinear load [37], [38]. However, the feeder impedance of a 1-km line is at least $0.2\ \Omega$ [6], which is much larger than output impedance. Second, the physical

feeder impedance is assumed to be dominantly inductive. This is true for high-voltage or medium-voltage networks, where the inductive component of line impedance is much higher than the resistive component. However, in low-voltage networks, though the resistive component of line impedance is dominant, series coupling chokes are normally installed in the droop-controlled DG units to improve system stability. Moreover, DG units are often interconnected to the PCC through a Δ/Y transformer to feed single-phase load. The isolation transformer introduces high inductive leakage impedance. Finally, even for some directly coupled DG units without coupling chokes or transformers, the virtual inductance can be preactivated through a virtual impedance control scheme to make the equivalent impedance dominantly inductive [19], [39]. Under these two assumptions, the distribution of Q_{UH} is mainly determined by feeder inductance.

To summarize this section, the fundamental negative sequence and harmonic current are not shared in a controllable manner if traditional droop alone is implemented. Instead, the distribution of Q_{UH} will be determined by feeder impedance. Consequently, such uncontrolled power distribution will lead to the overloading of a low-rated DG unit if it happens to be located close to the unbalanced and nonlinear load and is forced to take the majority of Q_{UH}. The direct way to share Q_{UH} is to tune the equivalent impedance of each DG unit to a common value.

III. PROPOSED ADAPTIVE VIRTUAL IMPEDANCE CONTROL METHOD

To realize the accurate sharing of unbalanced and harmonic power without involving any communication infrastructure or feeder impedance measurement, this paper proposes an adaptive virtual impedance control scheme based on the injection of an extra SACS as a link among DG units. The basic operating principle and key parts of the control scheme are comprehensively introduced as follows.

A. Basic Idea

As discussed in Section II, the direct way to tune the distribution of Q_{UH} is to regulate the equivalent series impedance seen by the load of each DG unit. Therefore, virtual impedance control is implemented at the fundamental negative sequence and selected harmonic frequencies to change the equivalent impedance. Under the assumption that feeder impedance is mainly inductive, a virtual inductor is added. Accordingly, the equivalent circuit of studied islanded microgrid at the fundamental negative sequence and harmonic frequencies with virtual inductance is shown in Fig. 5, where L_{v1} and L_{v2} represent virtual inductances. Clearly, L_v has negative correlation with Q_{UH} at the power stage of each DG unit; increase of L_v leads to decrease of Q_{UH}. The unbalanced and harmonic power can be equally shared only if (17) is fulfilled.

$$L_1 + L_{v1} = L_2 + L_{v2}. \qquad (17)$$

The difficult point is how to adaptively regulate the virtual inductance so as to make the equivalent impedance equal for each DG unit, without knowledge of the feeder inductance.
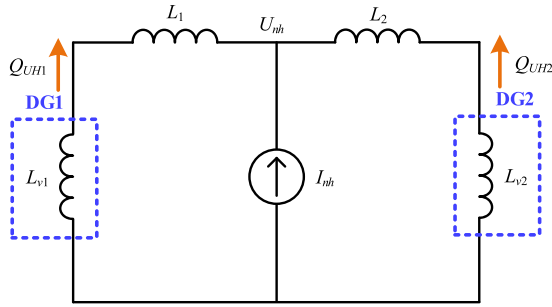
Fig. 5. Equivalent circuit of the studied islanded microgrid with proposed virtual impedance control in each DG unit presenting the fundamental negative sequence and harmonic frequency components.

As demonstrated in Section II-A, P–ω droop can realize equal active power sharing by utilizing frequency as a link among all DG units. Inspired by this characteristic, this paper proposes to build a similar droop relationship between the control target Q_{UH} and the frequency of an extra SACS that is injected in the output voltage of each DG unit. The proposed droop relationship is termed the Q_{UH}–ω_{ss} droop, and is mathematically expressed as

$$\omega_{ss}^* = \omega_{ss0} + k_{ss}Q_{UH} \tag{18}$$

where ω_{ss0} and ω_{ss}^* are, respectively, the nominal and reference angular frequency of the injected SACS; ω_{ss0} is set to be equal for every DG unit. k_{ss} is the droop coefficient, which is a positive value. The control scheme is not yet sufficient, because the control variable L_v and the injected signal have no relationship, meaning that the control loop is not yet closed. Hence, the second step is to adaptively regulate the virtual inductance according to the active power produced by the injected SACS. This coupling relationship between the SACS active power and the virtual inductance is termed the P_{ss}–L_v droop, and is expressed as

$$L_v = L_{v0} + k_L P_{ss} \tag{19}$$

where P_{ss} is the active power produced by the injected SACS; k_L is the coupling coefficient, which is defined as a positive value; and L_{v0} is the preactivated virtual inductance bias, which can be used to improve the X/R ratio of the feeder impedance or to enhance dynamic performance and stability of the DG inverter [39]. Since these issues are beyond the scope of this paper, the design of L_{v0} is not discussed, and L_{v0} is set to zero for simplicity.

Fig. 6 demonstrates the basic principle of the proposed control scheme. ω_1^* and ω_2^* represent the frequency of fundamental voltages. ω_{ss1}^* and ω_{ss2}^* represent the frequency of SACS voltages, which are determined by their respective Q_{UH} as in (18). L_{v1} and L_{v2} are the virtual inductances determined by (19), which are effective only at the fundamental negative sequence and selected harmonic frequencies. L_1 and L_2 are the physical feeder inductances. Note that the variables and relationships shown in blue are related with the fundamental negative sequence and harmonic frequencies; the variables and relationships shown in green are related with the SACS; and the relationships shown in red are realized in the proposed controller. To explain the power sharing mechanism, it is assumed that L_1 is larger than L_2 at

the start, and Q_{UH1} is smaller than Q_{UH2} based on the analysis shown in Fig. 5. With the proposed Q_{UH}–ω_{ss} droop control in (18), the frequency of the SACS ω_{ss1}^* should be smaller than ω_{ss2}^*. Then, the SACS phase angle of DG$_1$ decreases, and DG$_2$ increases. Thus, P_{ss1} decreases and P_{ss2} increases according to (6). Subsequently, L_{v1} decreases and L_{v2} increases according to (19). Consequently, Q_{UH1} increases and Q_{UH2} decreases. This negative-feedback closed loop adaptively regulates the virtual impedance to compensate the feeder impedance difference in each DG unit, and automatically realizes the unbalanced and harmonic power sharing. Moreover, the injected SACS of each DG unit will synchronize and reach a common frequency value at the steady state, ensuring that the Q_{UH} power sharing error can be completely compensated according to (18).

Similar to the coefficient design method in traditional droop control, if DG units have the same rating, then the coefficient of the Q_{UH}–ω_{ss} droop, i.e., k_{ss}, should be designed identically to achieve equal Q_{UH} sharing. However, when inverters with different power ratings are connected in parallel, k_{ss} for each DG unit should be designed according to the following relationship:

$$k_{ss1}S_1 = k_{ss2}S_2 = \cdots = k_{ssn}S_n. \tag{20}$$

In this way, the unbalanced and harmonic power can be distributed as per the kVA ratings of the different DG units. While considering the $P_{ss} - L_v$ droop coefficient, i.e., k_L, is related to system stability, the design method will be discussed in detail in Section IV.

In this proposed method, the active power and reactive power are still shared by the traditional P–ω and Q–E droop control. Fortunately, it can be noticed that the proposed $Q_{UH} - \omega_{ss}$ and $P_{ss} - L_v$ droop control are completely compatible with the traditional P–ω and Q–E droop control, because the frequency of the injected signal is different from the fundamental frequency, and the virtual inductance only functions at the fundamental negative sequence and harmonic frequencies. Therefore, the proposed control scheme will not deteriorate the power sharing performance of P–ω and Q–E droop control.

B. Overall Control Scheme

As shown in Fig. 7, the overall control scheme of the proposed method mainly comprises current signal extraction, power calculation, proposed droop control, virtual impedance implementation, and voltage regulation. The signal extraction block is responsible for separating the current component at the frequency of the injected SACS, the fundamental current component, and each selected harmonic current component from the output current. The power calculation block is used to compute the output active power, reactive power, unbalanced and harmonic power, and the active power produced by the injected SACS, based on the current components provided by the signal extraction block. In addition, the proposed droop control utilizes the powers calculated earlier to derive the fundamental voltage frequency and amplitude, frequency of the injected signal, and magnitude of virtual inductance based on the droop equations shown in (1), (2), (18), and (19). Furthermore, the virtual
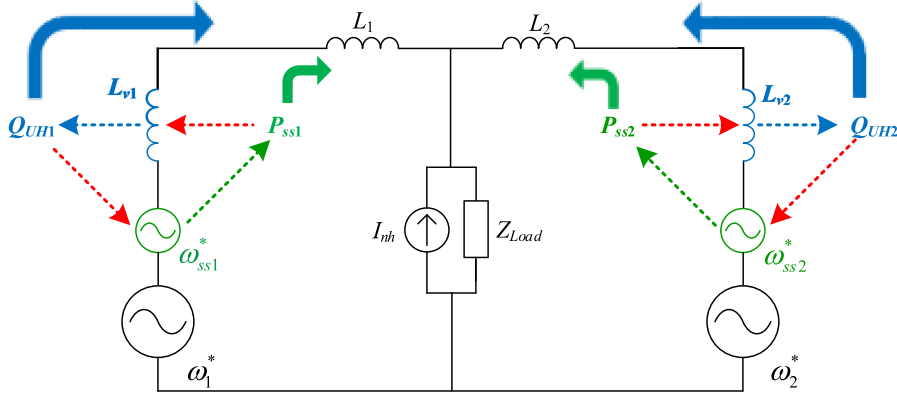
Fig. 6. Basic principle of the proposed adaptive virtual impedance control scheme for unbalanced and harmonic power sharing in islanded microgrids, where an extra ac voltage with the angular frequency of ω^*_{ssi} is generated at the output voltage of each DG unit for regulating the virtual inductance L_{vi}.
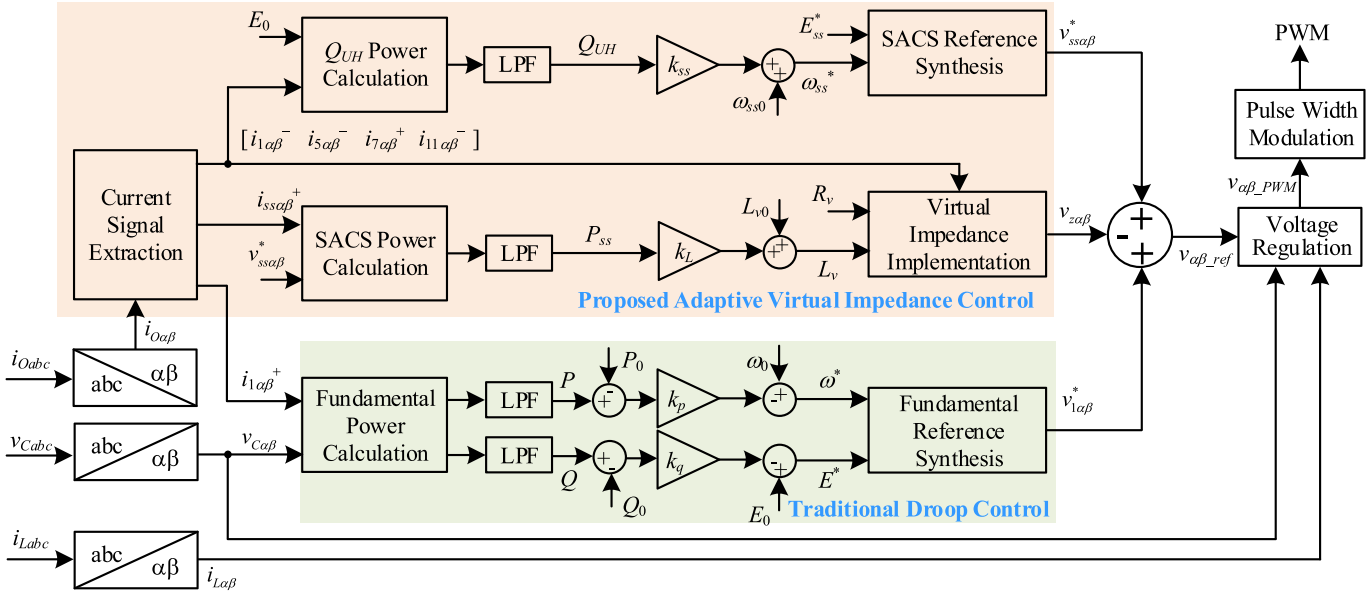

Fig. 7. Overall control block diagram of DG with the proposed adaptive virtual impedance control method for unbalanced and harmonic power sharing.

impedance implementation block computes the imaginary voltage drop on the virtual inductance. So, the total voltage reference can be calculated by adding the fundamental voltage reference and the SACS voltage reference, and subtracting the voltage drop on the virtual inductance. Finally, the voltage regulation based on multiple resonant controllers in the $\alpha\beta$ frame is employed to ensure the output voltage following the total voltage reference.

C. SACS Injection

To inject the SACS into the output voltage of each inverter, the reference voltage of the SACS is added to the total voltage reference. Meanwhile, a resonant controller, whose resonant frequency is adaptively adjusted to the frequency of the SACS, is employed in the voltage regulation. To avoid introducing excessive effect into the system, the frequency and amplitude of the injected SACS must be carefully designed.

1) Design of SACS Frequency: The frequency of the injected SACS is around ω_{ss0} and drifts slightly according to the output Q_{UH}, as shown in (18). Hence, the design of the rated frequency ω_{ss0} is important. To guarantee that the injected signal is well controlled and can be easily extracted but, meanwhile, does not deteriorate the output voltage quality, the following three rules should be considered.

Rule 1: The frequency of the injected signal should be within the bandwidth of the voltage control loop to avoid amplitude attenuation.

Rule 2: The frequency of the SACS should not be close to the frequencies of pre-existing signals in the system to avoid chaos; e.g., fundamental voltage frequency (50/60 Hz) and odd low-order harmonic frequencies introduced by nonlinear load should be avoided.
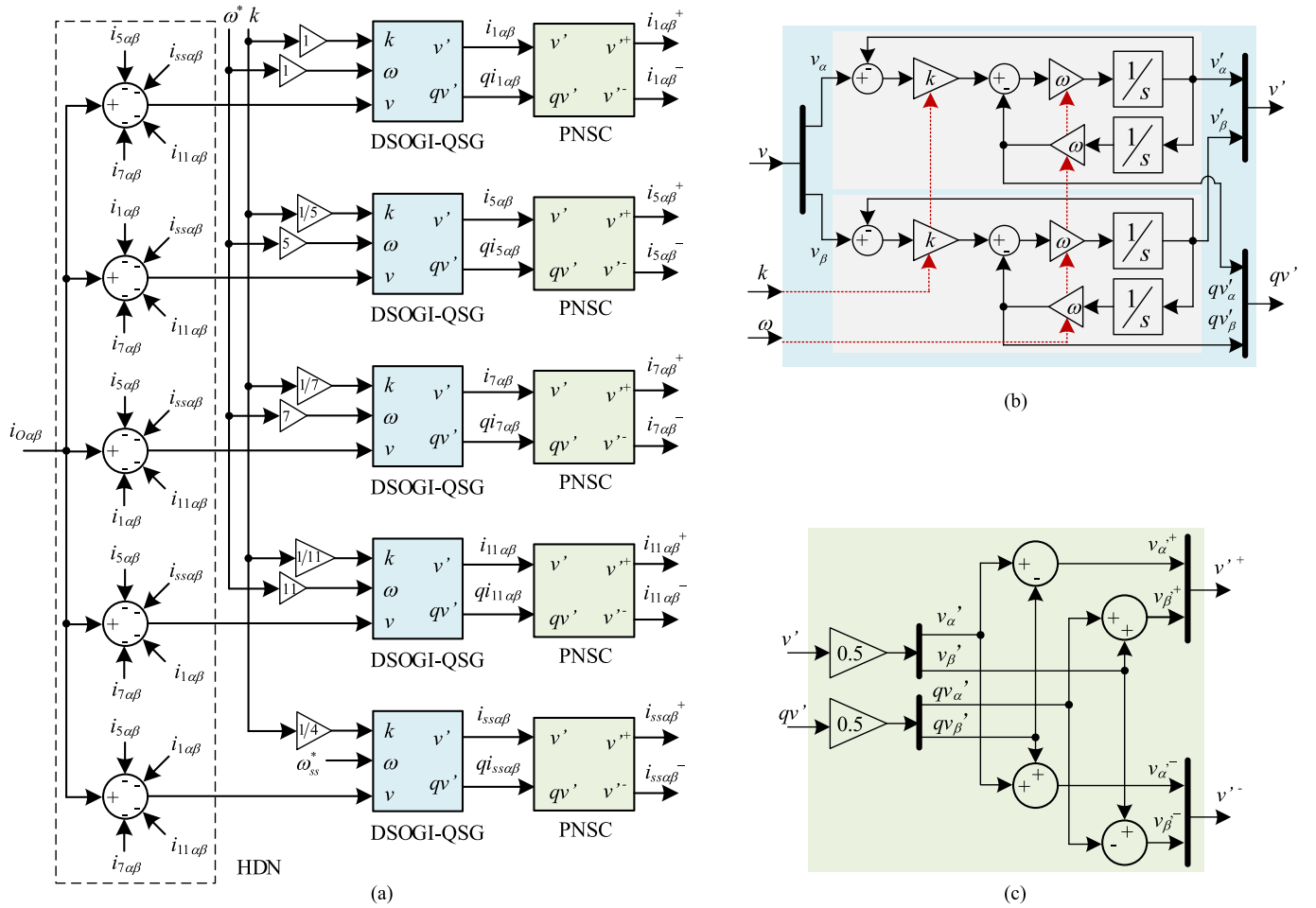
Fig. 8.   Block diagram of the current signal extraction used in the proposed scheme. (a) Overall framework. (b) Structure of DSOGI-QSG. (c) Structure of PNSC.

Rule 3:   The frequencies of interharmonics or subharmonics should not be used, since the voltage distortion limitations required by standards are usually more rigorous at interharmonics and subharmonics [40]

Therefore, in this paper, ω_{ss0} is set to four times the fundamental frequency, $2\pi \times 200$ rad/s, as an example.

2) Design of SACS Amplitude: The amplitude of the injected signal, denoted by E_{ss}^*, is a small constant value. The only point worth concerning for design of the amplitude is the tradeoff between signal extraction and the power quality limitation. Obviously, signals with large amplitude can ease signal extraction. However, power quality standards such as in [40] limit the total harmonic distortion (THD) in voltage within 8% and in individual harmonics within 5%. Therefore, it is recommended to design the amplitude of the SACS to be 0.5–2% of the fundamental voltage amplitude.

Once the frequency and amplitude are determined, the reference voltage of the injected SACS can be derived as

$$v_{ss\alpha}^* = E_{ss}^* \cos\left(\int \omega_{ss}^* \, dt\right) \tag{21a}$$

$$v_{ss\beta}^* = E_{ss}^* \sin\left(\int \omega_{ss}^* \, dt\right) \tag{21b}$$

where $v_{ss\alpha}^*$ and $v_{ss\beta}^*$ are, respectively, the α-axis and β-axis components of the SACS voltage reference.

D. Current Signal Extraction

To support the power calculation and virtual impedance implementation, a signal extraction method, based on multiple second-order generalized integrators (SOGIs) [41], is utilized to separate all of the required current components from the output current. The overall framework of the signal extraction algorithm is depicted in Fig. 8(a). First, a harmonic decoupling network, consisting of a cross-feedback structure, is used to isolate the interactions of different harmonics in the input current signal. Afterward, a number of dual SOGI quadrature signal generators (DSOGI-QSGs) are tuned at different frequencies and operate in parallel to separate different current components. Each DSOGI-QSG contains two SOGI-QSGs that are working on the α-axis and β-axis, respectively, as shown in Fig. 8(b). The transfer functions from the input signal v to the two in-quadrature output

signals v' and qv' of the SOGI-QSG are as follows:

$$D(s) = \frac{v'}{v}(s) = \frac{k\omega s}{s^2 + k\omega s + \omega^2} \tag{22}$$

$$Q(s) = \frac{qv'}{v}(s) = \frac{k\omega^2}{s^2 + k\omega s + \omega^2} \tag{23}$$

where ω is the resonant frequency, which is tuned at the frequency of the desired signal. The gain k determines the bandwidth of the SOGI-QSG. Considering the tradeoff between dynamic response and harmonic rejection, k is set to $\sqrt{2}$. As can be concluded from (22) and (23), the SOGI-QSG behaves as a bandpass filter, which only allows signal at a certain frequency of ω to pass. Moreover, the qv' output is always 90° lagged from the v' output. Therefore, for a three-phase unbalanced signal transformed to $\alpha\beta$ stationary reference frame, if its α-axis and β-axis components, i.e., v'_α and v'_β, and their corresponding in-quadrature signals, i.e., qv'_α and qv'_β, are obtained from the SOGI-QSG, then its instantaneous positive and negative sequence components can be separated by the positive–negative sequence calculation (PNSC) block shown in Fig. 8(c). v'^{+} and v'^{-} are the extracted positive and negative sequence components of the input signal, respectively.

Based on the signal extraction algorithm shown in Fig. 8, all of the desired current signals at different frequencies and sequences can be extracted. $i^{+}_{1\alpha\beta}$ is the fundamental positive sequence current used to calculate P and Q; $i^{+}_{ss\alpha\beta}$ is the positive sequence current at the injected SACS frequency, which is used to calculate P_{ss}. $i^{-}_{1\alpha\beta}$ is the fundamental negative sequence current; $i^{-}_{5\alpha\beta}$ is the 5th harmonic negative sequence current; $i^{+}_{7\alpha\beta}$ is the 7th harmonic positive sequence current; and $i^{-}_{11\alpha\beta}$ is the 11th harmonic negative sequence current. These instantaneous current components ($i^{-}_{1\alpha\beta}$, $i^{-}_{5\alpha\beta}$, $i^{+}_{7\alpha\beta}$, and $i^{-}_{11\alpha\beta}$) are the selected dominant components that contribute to Q_{UH} in the specific load condition studied in this paper. Therefore, they are used to calculate Q_{UH} and support virtual impedance control. Compared with other signal extraction methods, this multiple-SOGI-based algorithm has fast dynamic response and high accuracy, which makes it suitable for this application.

E. Power Calculation

With the detected current components in the previous section, the output active power, reactive power, unbalanced and harmonic power, and active power produced by the injected SACS of each inverter can be calculated as follows: eqn. (26) shown at the bottom of this page.

$$P = \frac{3}{2}\frac{\omega_{cp}}{(s + \omega_{cp})}\left(v_{C\alpha}i^{+}_{1\alpha} + v_{C\beta}i^{+}_{1\beta}\right) \tag{24}$$

$$Q = \frac{3}{2}\frac{\omega_{cp}}{(s + \omega_{cp})}\left(v_{C\beta}i^{+}_{1\alpha} - v_{C\alpha}i^{+}_{1\beta}\right) \tag{25}$$

$$P_{ss} = \frac{3}{2}\frac{\omega_{cp}}{(s + \omega_{cp})}\left(v^{*}_{ss\alpha}i^{+}_{ss\alpha} + v^{*}_{ss\beta}i^{+}_{ss\beta}\right) \tag{27}$$

where $v_{C\alpha}$ and $v_{C\beta}$ are the measured instantaneous capacitor voltages in the stationary reference frame derived by Clarke transformation; s is the Laplace operator; and ω_{cp} is the cutoff frequency for the LPFs, which are used to attenuate the ripples in the calculated powers. The cutoff frequency for LPFs is set very low to achieve good attenuation of ripples and to avoid interaction with the voltage regulation loop [42], [43]. In this paper, the cutoff frequency of LPFs is set to 5 Hz.

Similar to the calculation of Q_{UH}, the reference voltage rather than the actual output voltage of the SACS is used to calculate P_{ss}. This approximation saves signal extraction of the SACS voltage but will not introduce significant calculation errors; hence, a more concise control structure is obtained.

F. Virtual Impedance Implementation

The virtual inductance is adaptively regulated by the SACS active power as shown in (19). Once the virtual inductance is determined, its corresponding voltage drops at different frequencies and sequences can be calculated. The algebraic-type virtual impedance implementation method introduced in [19], [39], and [44] is adopted in this paper, where the phase shift of virtual inductance can be easily attained by the cross-coupling feedback of the current vector in the two-axis stationary reference frame. The voltage drops at the fundamental negative sequence and each selected harmonic frequency can be calculated by

$$\begin{bmatrix} v^{-}_{1\alpha} \\ v^{-}_{1\beta} \end{bmatrix} = \begin{bmatrix} R_{v1} & \omega^{*}L_v \\ -\omega^{*}L_v & R_{v1} \end{bmatrix} \begin{bmatrix} i^{-}_{1\alpha} \\ i^{-}_{1\beta} \end{bmatrix} \tag{28}$$

$$\begin{bmatrix} v^{-}_{5\alpha} \\ v^{-}_{5\beta} \end{bmatrix} = \begin{bmatrix} R_{v5} & 5\omega^{*}L_v \\ -5\omega^{*}L_v & R_{v5} \end{bmatrix} \begin{bmatrix} i^{-}_{5\alpha} \\ i^{-}_{5\beta} \end{bmatrix} \tag{29}$$

$$\begin{bmatrix} v^{+}_{7\alpha} \\ v^{+}_{7\beta} \end{bmatrix} = \begin{bmatrix} R_{v7} & -7\omega^{*}L_v \\ 7\omega^{*}L_v & R_{v7} \end{bmatrix} \begin{bmatrix} i^{+}_{7\alpha} \\ i^{+}_{7\beta} \end{bmatrix} \tag{30}$$

$$\begin{bmatrix} v^{-}_{11\alpha} \\ v^{-}_{11\beta} \end{bmatrix} = \begin{bmatrix} R_{v11} & 11\omega^{*}L_v \\ -11\omega^{*}L_v & R_{v11} \end{bmatrix} \begin{bmatrix} i^{-}_{11\alpha} \\ i^{-}_{11\beta} \end{bmatrix} \tag{31}$$

where L_v is the desired virtual inductance given by (19), and ω^{*} is the fundamental frequency reference determined by the P–ω droop in (1). Additionally, R_{v1}, R_{v5}, R_{v7}, and R_{v11} are the small virtual resistances implemented at the fundamental negative sequence and each selected harmonic frequency to provide a damping effect to the system [45]. Nevertheless, the design for system damping is beyond the scope of this paper. $v^{-}_{1\alpha\beta}$, $v^{-}_{5\alpha\beta}$, $v^{+}_{7\alpha\beta}$, and $v^{-}_{11\alpha\beta}$ are the calculated instantaneous voltage drops for virtual impedance at the selected compensation frequencies.

Finally, the total voltage drop for the virtual impedance is obtained by adding all of the components calculated earlier as

$$Q_{UH} = \frac{3E_0}{2}\frac{\omega_{cp}}{(s + \omega_{cp})}\sqrt{(i^{-}_{1\alpha})^2 + (i^{-}_{1\beta})^2 + (i^{-}_{5\alpha})^2 + (i^{-}_{5\beta})^2 + (i^{+}_{7\alpha})^2 + (i^{+}_{7\beta})^2 + (i^{-}_{11\alpha})^2 + (i^{-}_{11\beta})^2} \tag{26}$$
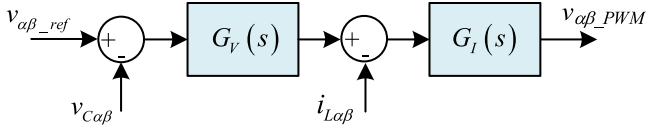
Fig. 9.   Block diagram of the voltage regulation in the proposed scheme.

follows:

$$v_{z\alpha} = v_{1\alpha}^- + v_{5\alpha}^- + v_{7\alpha}^+ + v_{11\alpha}^- \tag{32a}$$

$$v_{z\beta} = v_{1\beta}^- + v_{5\beta}^- + v_{7\beta}^+ + v_{11\beta}^- \tag{32b}$$

where $v_{z\alpha}$ and $v_{z\beta}$ are the voltage drops for the required virtual impedance in the stationary reference frame. This voltage drop is deducted from the reference voltage to emulate the effect of actual impedance. It should be noted that this virtual impedance implementation method does not involve any differential operations. Therefore, it will not bring high-frequency noise amplification issues.

G. Voltage Regulation

The proposed adaptive virtual impedance and droop control comprise the power control loop that generates the voltage reference for the voltage control loop. The reference voltage is obtained by adding the fundamental voltage reference in (3) and the SACS voltage reference in (21), and then subtracting the voltage drop for the virtual impedance in (32), as follows:

$$v_{\alpha\_ref} = v_{1\alpha}^* + v_{ss\alpha}^* - v_{z\alpha} \tag{33a}$$

$$v_{\beta\_ref} = v_{1\beta}^* + v_{ss\beta}^* - v_{z\beta} \tag{33b}$$

where v_{α_ref} and v_{β_ref} are the total voltage references in the stationary reference frame given by the power control loop.

To achieve excellent reference voltage tracking, a dual-loop voltage regulation structure as shown in Fig. 9 is adopted. The outer loop is an *LC* filter capacitor voltage control loop with a PR controller, and the inner loop is an inductor current control loop with a proportional controller [19], [46]. The voltage regulators for the dual-loop are expressed as

$$G_V(s) = k_{pV} + \sum_{h=1,5,7,11} \frac{2k_{ih}\omega_c s}{s^2 + 2\omega_c s + (h\omega^*)^2}$$
$$+ \frac{2k_{iss}\omega_c s}{s^2 + 2\omega_c s + (\omega_{ss}^*)^2} \tag{34}$$

$$G_I(s) = k_{pI} \tag{35}$$

where $G_V(s)$ and $G_I(s)$ are the transfer functions of voltage regulator and current regulator, respectively; k_{pV} is the gain of voltage proportional controller; k_{ih} and k_{iss} are the gains of each resonant controller; ω_c is the cutoff frequency of the resonant controllers; and k_{pI} is the gain of current proportional controller. As can be noticed from (34), an independent resonant controller whose resonant frequency is set at the frequency of the SACS is applied to guarantee excellent tracking of the SACS reference voltage. Moreover, since the frequencies are determined by the droop equations in (1) and (18), and may deviate from

their rated values, the proposed PR controllers should adaptively adjust their resonant frequencies. It should be noted that the proportional controller in the inner current control loop is used to increase internal stability and to provide overcurrent protection.

Compared with the existing unbalanced and harmonic power sharing control methods, the proposed adaptive virtual impedance control method achieves four advantages.

1) Unbalanced and harmonic power can be equally shared among DG units, or proportionally shared according to power ratings.
2) This control scheme is only based on the local variable and is totally distributed, so no communication link or central controller is needed, and thus the plug-and-play feature is ensured.
3) It is not necessary to know feeder impedances in advance.
4) The voltage control loop is not varied with the active power of SACS, and the dynamic performance and system stability are less impacted by unbalanced and harmonics power sharing.

IV. PARAMETER DESIGN AND STABILITY ANALYSIS

In this proposed power sharing control method, two control parameters must be determined, i.e., k_{ss} and k_L. This section expands on the design methodology of k_{ss} and k_L based on the modeling of the studied islanded microgrid system. The stability analysis of the proposed control method is also provided. Because Q_{UH} is independent of P and Q, and the model for traditional droop control is already well established in existing publications [42], [43], the model built in this paper only considers the effect of the injected SACS and virtual inductance.

A. Design of Coupling Coefficient k_L

To design a proper value for k_L, the steady-state operating point of the proposed control method is needed. First, it is assumed that the system has already reached steady state, meaning that the frequency of the SACS in each DG unit has synchronized to a common value and Q_{UH} has been equally shared between two DG units according to (18). In other words, $\omega_{ss1} = \omega_{ss2}$ and $Q_{UH1} = Q_{UH2}$ are realized. Furthermore, the equivalent impedances of DG1 and DG2 are equal, as in (17). Then, the difference between L_{v1} and L_{v2} is deduced as

$$L_{v1} - L_{v2} = L_2 - L_1. \tag{36}$$

In addition, the active power produced by the SACS of each DG unit has the following relationship:

$$P_{ss1} + P_{ss2} = P_{ssL} \tag{37}$$

where P_{ssL} is the SACS active power absorbed by the load. It should be noted that P_{ssL} can be regarded as a constant value if the load does not change. Based on (19) and (37), the following relationship is derived if L_{v0} is designed to be zero:

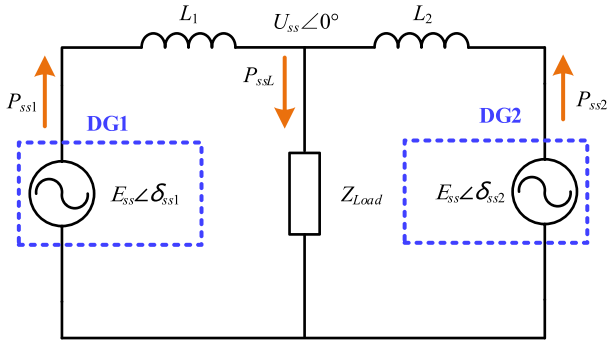$$L_{v1} + L_{v2} = k_L (P_{ss1} + P_{ss2}) = k_L P_{ssL}. \tag{38}$$

Fig. 10. Equivalent circuit of the studied islanded microgrid presenting components at the frequency of injected SACS.

Fig. 11. Variation of active power with phase angle in each DG unit at the frequency of injected SACS.

Finally, combining (36) and (38), the virtual inductance of each DG unit at steady state can be calculated as

$$L_{v1} = \frac{P_{ssL}k_L}{2} + \frac{L_2 - L_1}{2} \quad (39a)$$

$$L_{v2} = \frac{P_{ssL}k_L}{2} - \frac{L_2 - L_1}{2}. \quad (39b)$$

Meanwhile, the output active power produced by the SACS of each DG unit at steady state is derived according to (19).

$$P_{ss1} = \frac{P_{ssL}}{2} + \frac{L_2 - L_1}{2k_L} \quad (40a)$$

$$P_{ss2} = \frac{P_{ssL}}{2} - \frac{L_2 - L_1}{2k_L}. \quad (40b)$$

It can be seen that the steady state values for virtual inductance and the SACS active power are related to the coupling coefficient. The virtual inductance is proportional to k_L. Assuming that L_2 is larger than L_1, P_{ss1} decreases with the increase of k_L, but P_{ss2} increases. To ensure that the virtual inductance and the SACS active power are limited to a reasonable range, two design criteria of k_L are built as follows.

Criterion 1: Limitation of Power Angle Stability

Similar to the equivalent circuit at fundamental positive sequence in Fig. 3, the equivalent circuit at the frequency of the SACS can be derived as shown in Fig. 10. Taking DG1 as an example, the output SACS active power of DG1 can be expressed as

$$P_{ss1} = \frac{E_{ss}U_{ss}}{X_1}\sin\delta_{ss1} \quad (41)$$

where U_{ss} represents the SACS voltage at the PCC and δ_{ss1} is the phase angle of DG1. The variation of SACS active power with phase angle is depicted in Fig. 11. It can be seen that the active power varies as a sinusoidal wave of the angle: a highly nonlinear relationship. When the angle is smaller than 90° (e.g., point *a*), the active power increases along with the angle. However, a further increase in angle results in a decrease in power when the angle is larger than 90° (e.g., point *b*). According to the power angle stability criteria in the power system, a necessary condition for ensuring that all DG units remain in synchronism and operate stably is to keep the angle below 90° [47]. To evaluate
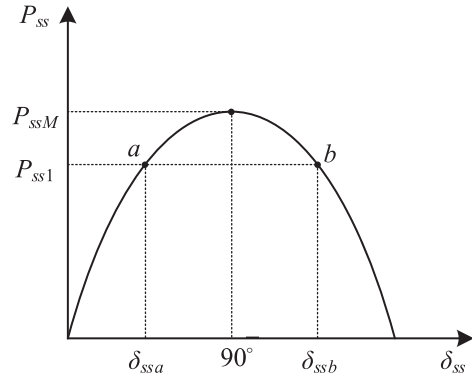
the degree of angle stability, the stability reservation coefficient K_P is defined as

$$K_P = \frac{P_{ssM} - P_{ss1}}{P_{ss1}} \times 100\% \quad (42)$$

where P_{ssM} is the maximum transferred power when δ_{ss} equals 90°. The increase of K_P results in a larger angle stability margin, whereas the transferred power will decrease. In power system design guides such as [48], K_P is recommended to be at least 20% to retain a sufficient stability margin. However, different from a power system, the principal function of the SACS is to establish a link among DG units instead of transferring power, so K_P can be designed larger than that in a power system to guarantee a large enough stability margin. Based on this experience, K_P larger than 40% is recommended in this control method. Thus, the upper limit for SACS active power is obtained:

$$P_{ss1} < \frac{P_{ssM}}{1.4}. \quad (43)$$

By substituting (40a) into (43), the minimum value for the coupling coefficient, k_L, is determined as in (44). To simplify the calculation, U_{ss} can be assumed to be equal to E_{ss}.

$$k_L > \frac{0.7X_1(L_2 - L_1)}{E_{ss}U_{ss} - 0.7X_1P_{ssL}}. \quad (44)$$

Criterion 2: Limitation of PCC Voltage THD

Considering the simplified equivalent circuit at the fundamental negative sequence and harmonic frequencies as shown in Fig. 5, the distortion voltage at PCC, i.e., U_{nh}, is determined by the load distortion current and the equivalent inductance of both DG units. The system equivalent inductance, denoted by L_e, is defined as the parallel inductance of DG1 and DG2. Clearly, U_{nh} is proportional to L_e under a specific load condition. Before the virtual inductance is implemented, the system equivalent inductance can be expressed as

$$L_e = \frac{L_1L_2}{L_1 + L_2}. \quad (45)$$

After the virtual inductance is implemented, the system equivalent inductance becomes

$$L'_e = \frac{(L_1 + L_{v1})(L_2 + L_{v2})}{L_1 + L_{v1} + L_2 + L_{v2}}. \tag{46}$$

By substituting (39) into (46), the system equivalent inductance at steady state is obtained:

$$L'_e = \frac{P_{ssL}k_L}{4} + \frac{L_1 + L_2}{4}. \tag{47}$$

It can be noted that the system equivalent inductance has a proportional relationship with k_L based on (47). Therefore, the coupling coefficient k_L should be designed to be small enough to ensure that the voltage THD at the PCC does not exceed the required limitation.

In addition, it can be mathematically proven that L'_e is always larger than L_e, which means that the virtual inductance will slightly increase the voltage distortion at the PCC compared with the traditional droop control method. This issue can be avoided only when a negative virtual inductance is inserted for every DG unit. However, it is difficult to find a proper negative virtual inductance to realize power sharing without communication among DG units or knowledge of the feeder impedance. Under such conditions, a feasible solution is to design k_L to be small enough so that the increase of voltage THD can be limited within an acceptable range. Furthermore, the injected SACS will also increase the voltage distortion at its own frequency, as mentioned in Section III-C. Fortunately, this effect can be restricted below the grid code requirement if E^*_{ss} and k_L are designed carefully.

Based on the aforementioned discussion, it can be concluded that there exists a compromise relationship between PCC voltage quality and power angle stability when designing k_L. Therefore, both Criteria 1 and 2 must be considered concurrently.

B. Design of Droop Coefficient k_{ss}

In this section, a small-signal linearization model for the proposed control scheme is built to analyze system stability and to derive the design methodology for droop coefficient k_{ss}. The objective of the modeling process is to derive a closed loop for the unbalanced and harmonic power sharing error. Since the bandwidth of the proposed power controller is far lower than the bandwidth of the voltage controller, the dynamic characteristic of the voltage regulation can be ignored. By introducing a small perturbation around the equilibrium operating point, the following small-signal linearization model is obtained, where the symbol "^" indicates the perturbation signal.

First, the system model at the frequency of the injected SACS as shown in Fig. 10 is analyzed. Assuming that a small load power perturbation $\hat{Q}_{UH}$ is introduced around the steady-state operating point, the following equations are obtained:

$$\hat{\omega}_{ss1} = k_{ss}\hat{Q}_{UH1} \tag{48a}$$

$$\hat{\omega}_{ss2} = k_{ss}\hat{Q}_{UH2} \tag{48b}$$

$$\Delta\hat{\omega}_{ss} = \hat{\omega}_{ss1} - \hat{\omega}_{ss2} = k_{ss}(\hat{Q}_{UH1} - \hat{Q}_{UH2}) = -k_{ss}\Delta\hat{Q}_{UH}. \tag{49}$$

The SACS frequency difference leads to the phase angle difference between DG1 and DG2 of

$$\hat{\delta}_{ss} = \hat{\delta}_{ss1} - \hat{\delta}_{ss2} = \frac{\Delta\hat{\omega}_{ss}}{s} = -\frac{k_{ss}}{s}\Delta\hat{Q}_{UH}. \tag{50}$$

Since P_{ssL} is determined by U_{ss}, which is independent of phase angle perturbation, P_{ssL} can be regarded as a constant value, meaning that the SACS active power perturbation signal only flows between DG units. Therefore, the SACS active power perturbation signals of DG1 and DG2 have the following relationship:

$$\hat{P}_{ss1} = -\hat{P}_{ss2} = \frac{E^2_{ss}}{X_1 + X_2}\sin\hat{\delta}_{ss} \approx \frac{E^2_{ss}\hat{\delta}_{ss}}{X_1 + X_2}. \tag{51}$$

Furthermore, based on (19), (37), and (51), the small perturbation signals of virtual inductance for DG1 and DG2 have the following relationship:

$$\Delta\hat{L}_v = \hat{L}_{v1} - \hat{L}_{v2} = k_L\left(\hat{P}_{ss1} - \hat{P}_{ss2}\right) = 2k_L\hat{P}_{ss1}. \tag{52}$$

Next, the system model for unbalanced and harmonic power, as shown in Fig. 5, is analyzed. The distribution of the unbalanced and harmonic power at steady state is

$$Q_{UH1} = Q_{UHL}\frac{L_2 + L_{v2}}{L_1 + L_{v1} + L_2 + L_{v2}} \tag{53a}$$

$$Q_{UH2} = Q_{UHL}\frac{L_1 + L_{v1}}{L_1 + L_{v1} + L_2 + L_{v2}} \tag{53b}$$

where Q_{UHL} represents the load total unbalanced and harmonic power. Hence, the power distribution error between DG1 and DG2 is deduced as

$$\Delta Q_{UH} = Q_{UH2} - Q_{UH1}$$
$$= Q_{UHL}\left(\frac{L_1 - L_2}{L_1 + L_2 + k_L P_{ssL}} + \frac{L_{v1} - L_{v2}}{L_1 + L_2 + k_L P_{ssL}}\right). \tag{54}$$

The small-signal perturbation relationship in (54) can be derived as

$$\Delta\hat{Q}_{UH} = \frac{Q_{UHL}}{L_1 + L_2 + k_L P_{ssL}}\Delta\hat{L}_v = K\Delta\hat{L}_v \tag{55}$$

where $K = Q_{UHL}/(L_1 + L_2 + k_L P_{ssL})$ is a constant value once k_L is determined.

The complete model of the proposed power sharing control method is obtained by combining (49)–(52) and (55) as illustrated in Fig. 12, where the unbalanced and harmonic power sharing error $\Delta\hat{Q}_{UH}$ is treated as the controlled variable. In the steady state, the proposed power control scheme should compensate the power sharing error to zero. Thus, the reference value of the control loop is set to zero. Note that the dynamic characteristic of the signal extraction block is not considered in this model. This is because the cutoff frequency of the LPFs for calculating P_{ss} and Q_{UH} is selected at a relatively low level (5 Hz), as mentioned in Section III-E. Compared with the slow dynamics of LPFs, the dynamic of the signal extraction block can be ignored. Therefore, only two LPF blocks with cutoff frequency ω_{cp} are considered.
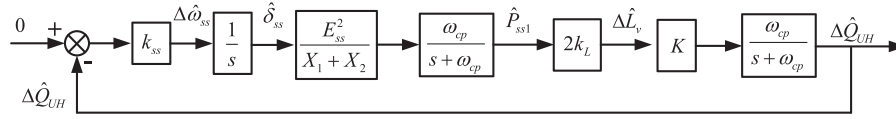
Fig. 12.   Small-signal model of the islanded microgrid with the proposed adaptive virtual impedance control method, covering the dynamic of injected SACS, unbalanced and harmonic power, and virtual inductance variation.

TABLE I
PARAMETERS OF THE STUDIED ISLANDED MICROGRID IN SIMULATIONS AND EXPERIMENTS

Symbol	Description	Simulation	Experiment
V_{dc}	DC voltage (V)	600	600
S	Capacity of DG (kVA)	N/A	9
f_s	Switching frequency (kHz)	12.5	12.5
L_f	Filter inductance (mH)	3	3
C_f	Filter capacitance (μF)	30	30
L_1+R_1	Feeder impedance of DG$_1$ (mH+Ω)	1+0.2	Case one, 1.2+0.2; Case two, 2.8+0.2
L_2+R_2	Feeder impedance of DG$_2$ (mH+Ω)	4+0.2	2.8 mH+0.2 Ω
R_{L1}	Balanced load (Ω)	40	40
R_{L2}	Unbalanced load (Ω)	20	20
$L_{L1}+R_{L3}$	Rectifier load (mH+Ω)	6+30	6+30
k_{p1}	*P-ω* droop coefficient of DG1 (rad/s/W)	6e-5	Case one, 6e-5; Case two, 1.2e-4
k_{p2}	*P-ω* droop coefficient of DG2 (rad/s/W)	6e-5	Case one, 6e-5; Case two, 6e-5
k_{q1}	*Q-E* droop coefficient of DG1 (V/var)	6e-6	Case one, 8e-5; Case two, 1.6e-4
k_{q2}	*Q-E* droop coefficient of DG2 (V/var)	6e-6	Case one, 8e-5; Case two, 8e-5
ω_0	Nominal fundamental frequency (rad/s)	100π	100π
E_0	Nominal fundamental phase voltage magnitude (V)	163	163
P_0	Nominal real power (kW)	2	Case one, 2; Case two, 0
Q_0	Nominal reactive power (kvar)	1	Case one, 1; Case two, 0
k_{dd1}	Direct droop coefficient of DG1 (H/var)	N/A	Case one, 1e-6; Case two, 2e-6
k_{dd2}	Direct droop coefficient of DG2 (H/var)	N/A	Case one, 1e-6; Case two, 1e-6
k_{ss1}	Q_{UH}-ω_{ss} droop coefficient of DG1 (rad/s/var)	0.015	Case one, 6e-4; Case two, 1.2e-3
k_{ss2}	Q_{UH}-ω_{ss} droop coefficient of DG2 (rad/s/var)	0.015	Case one, 6e-4; Case two, 6e-4
k_L	P_{ss}-L_v coupling coefficient (H/W)	4e-3	3e-3
ω_{ss0}	Nominal SACS frequency (rad/s)	400π	400π
E_{ss}^*	SACS magnitude reference (V)	1.15	1.63
ω_{cp}	Cutoff frequency of the LPFs for power calculation (rad/s)	31	31

Based on the small-signal linearization model derived earlier, the open-loop transfer function of the model can be deduced as

$$T(s) = \frac{2KE_{ss}^2 k_L \omega_{cp}^2}{X_1 + X_2} \frac{k_{ss}}{s(s+\omega_{cp})^2} = k_{ss} \frac{G}{s(s+\omega_{cp})^2} \quad (56)$$

where $G = 2KE_{ss}^2 k_L \omega_{cp}^2/(X_1 + X_2)$ is a constant once k_L is determined, and k_{ss} functions as the gain of the open-loop transfer function. Next, under simulation parameters listed in Table I, the root loci map of the closed-loop transfer function and Bode diagram of open-loop transfer function can be constructed as shown in Figs. 13 and 14, respectively. Based on Fig. 13, it can

be seen that when k_{ss} increases, two roots of the closed-loop system move to the right-half plane, meaning that system becomes unstable. In Fig. 14, four Bode plots are illustrated under four different k_{ss} values (0.001, 0.05, 0.1, and 0. 2). Their phase curves overlap with each other. However, their amplitude curves move up with the increase of k_{ss}, which means that the control loop bandwidth is increased but stability margin is decreased. To maintain stability, the upper limit value of k_{ss} can be obtained by
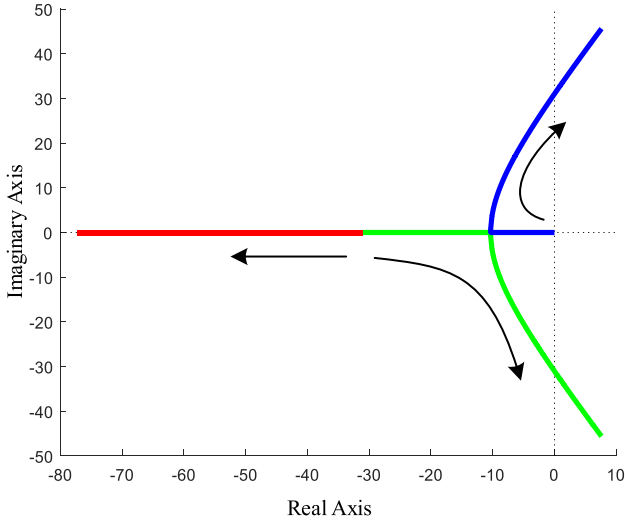
$$k_{ss} < \frac{2\omega_{cp}^3}{G}. \quad (57)$$

Fig. 13. Root loci of the closed-loop transfer function of the small-signal model where droop coefficient k_{ss} changes from 0 to 0.3.
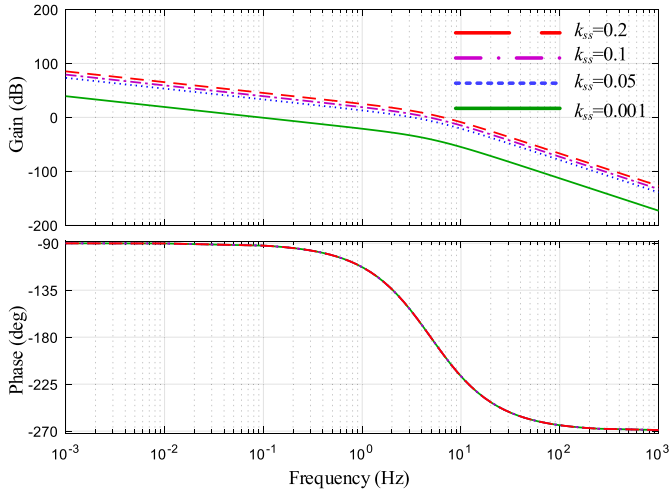

Fig. 14. Bode diagram of the open-loop transfer function of the small-signal model where coupling coefficient k_{ss} is equal to 0.001, 0.05, 0.1, and 0.2, respectively.

Criterion 3: Tradeoff Between Stability and Dynamic Response

According to the small-signal perturbation model derived earlier, there exists a tradeoff relationship between system stability and control loop bandwidth when designing k_{ss}. As k_{ss} deceases, the stability margin is increased. However, the bandwidth of the control loop is also decreased, resulting in slow dynamic response. Instead, increasing k_{ss} can widen the control bandwidth. However, system instability may also appear. Considering that the power sharing issue is a steady-state requirement, it is not necessary for the dynamic response to be fast. Therefore, ensuring system stability is a higher priority when designing k_{ss}. Afterward, dynamic response can be considered.

Based on the aforementioned discussion, the control parameter design procedure is given by considering Criteria 1–3 concurrently. First, k_L is determined by following Criteria 1 and 2 to fulfill both the power angle stability and the PCC voltage quality

requirement. Afterward, k_{ss} can be designed according to Criterion 3 to ensure system stability and dynamic response. Note that all of the parameter design analyses are based on a system with only two inverters. Therefore, the control parameters, for a simple system with two DG units, can be directly determined based on the equations and model derived earlier. However, when multiple DG units are connected, or some parameters in the model are unknown, it is difficult to directly calculate the control parameters. Under these circumstances, Criteria 1–3 drawn earlier still hold, and the control parameters can be tuned by the trial-and-error method accordingly.

V. SIMULATION AND EXPERIMENTAL RESULTS

To verify the effectiveness of the proposed method, simulations and experiments are conducted based on the same topology as shown in Fig. 1. Generalized load conditions, including a balanced load, an unbalanced load, and a rectifier load, are considered. The unbalanced load is connected between phases A and B. The detailed electrical setup and control system parameters for both simulations and experiments are listed in Table I. The simulation results based on PSCAD/EMTDC platform are provided to verify not only the power sharing performance, but also the parameter design methodology and modeling results introduced in Section IV, because some of the variables are difficult to measure in hardware experiments. Comprehensive experimental results based on a three-phase microgrid prototype with two DG units are also presented to validate the power sharing performance of the proposed method.

A. Simulation Results

At the beginning of the simulation, only the traditional droop control method is implemented before 2.0 s. Then the proposed adaptive virtual impedance control scheme is activated at 2.0 s. First, the power sharing performance of the proposed control scheme is verified by demonstrating the Q_{UH} waveform and each order harmonic current. Afterward, the coupling coefficient and droop coefficient are set to different values, respectively, to study their effect and verify the parameter design criteria introduced in Section IV.

1) Power Sharing Performance Verification: In this simulation case, k_L and k_{ss} for both DG units are, respectively, set to 0.004 and 0.015 (optimized control parameters given by the parameter design criteria). Before 2.0 s, the frequency of the injected SACS is fixed to its rated value (200 Hz) and the virtual inductance is forced to zero. Therefore, the proposed control scheme is disabled and only the traditional droop control is implemented. Afterward, the proposed scheme is enabled by adjusting SACS frequency according to (18) and adaptively tuning virtual inductance according to (19). The corresponding waveforms of unbalanced and harmonic power, SACS frequency, SACS active power, and virtual inductance are shown in Fig. 15. According to Fig. 15(a), it can be seen that the load Q_{UH} power is distributed based on feeder impedance before 2.0 s, but evenly shared by DG1 and DG2 when the proposed method is activated. The frequency of the injected SACS in Fig. 15(b), as expected, can reach to a common value after a short
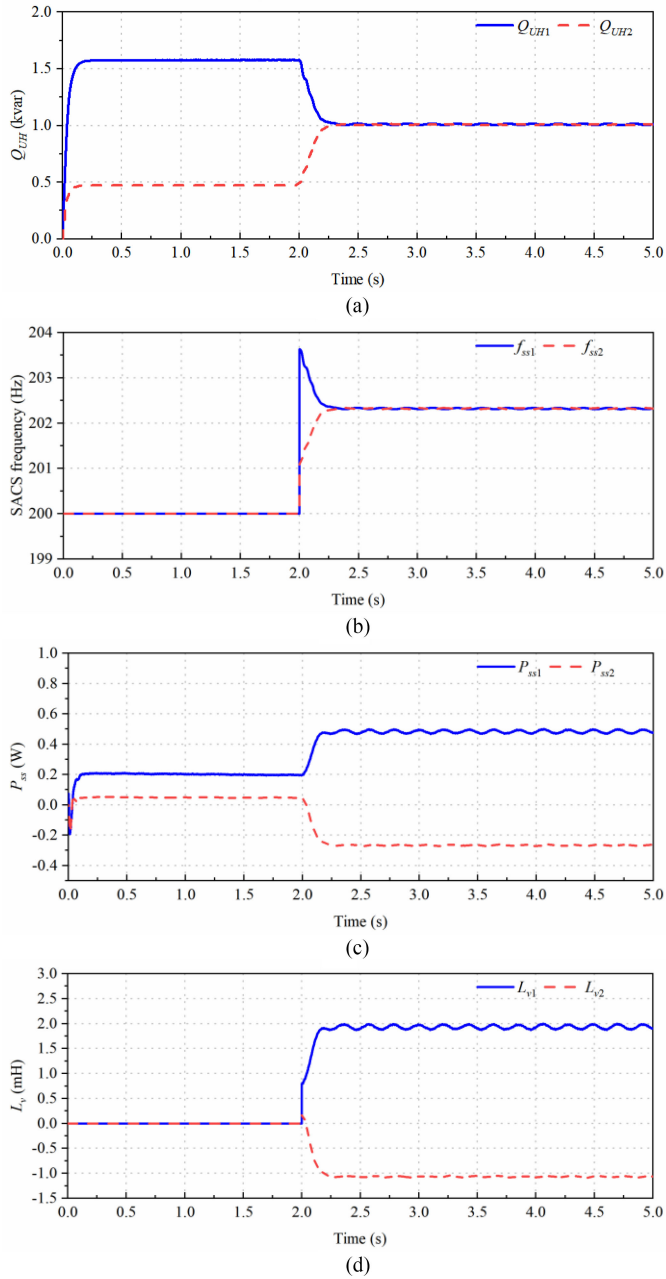
Fig. 15. Simulated waveforms of (a) output unbalanced and harmonic power, (b) SACS frequency, (c) SACS active power, and (d) virtual inductance of DG1 and DG2 where the proposed control scheme is activated at 2.0 s.
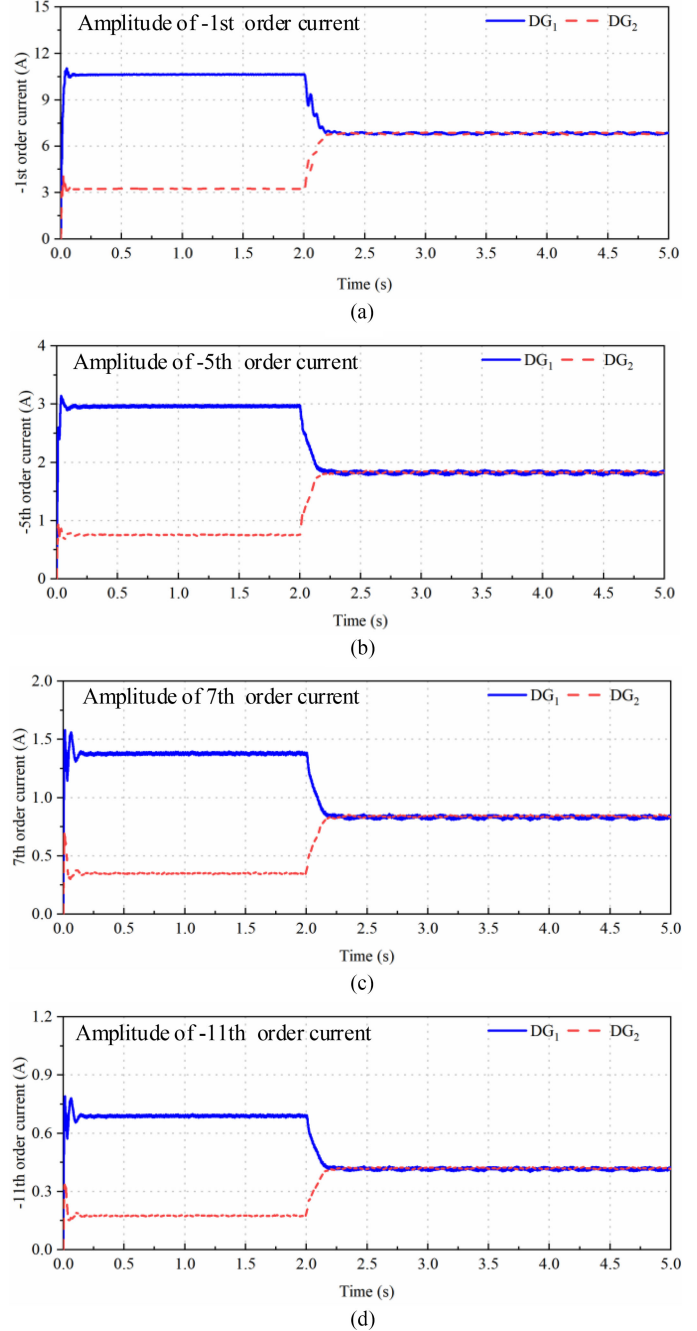

Fig. 16. Simulated waveforms of the amplitude of each order harmonic current. (a) Fundamental negative sequence current. (b) Fifth-order negative sequence harmonic current. (c) Seventh-order positive sequence harmonic current. (d) Eleventh-order negative sequence harmonic current.

period of dynamic process. The virtual inductances for DG1 and DG2, in steady state, are about 2 and -1 mH, respectively, which can exactly compensate the line inductance difference. Therefore, the condition in (17) is fulfilled and Q_{UH} is equally shared.

To fully verify the validity of the proposed scheme, the amplitude of each order harmonic current obtained by the signal extraction block is demonstrated in Fig. 16. It can be noticed that not only the total harmonic and unbalanced power, but also each order harmonic current compensated by the proposed scheme can be evenly shared.

2) k_L Design Methodology Verification: In this simulation case, the effect of the coupling coefficient on the system performance is investigated. By substituting the simulation parameters listed in Table I into (44), the minimum value for k_L to fulfill power angle stability is 0.0023. Therefore, k_L is set to 0.002, 0.004, 0.005, and 0.006, respectively, to verify Criteria 1 and 2. Meanwhile, k_{ss} is fixed at 0.015 during this process. The output Q_{UH} values of DG1 and DG2 are shown in Fig. 17. It can be seen that the system is stable when k_L is set to 0.004, 0.005, and
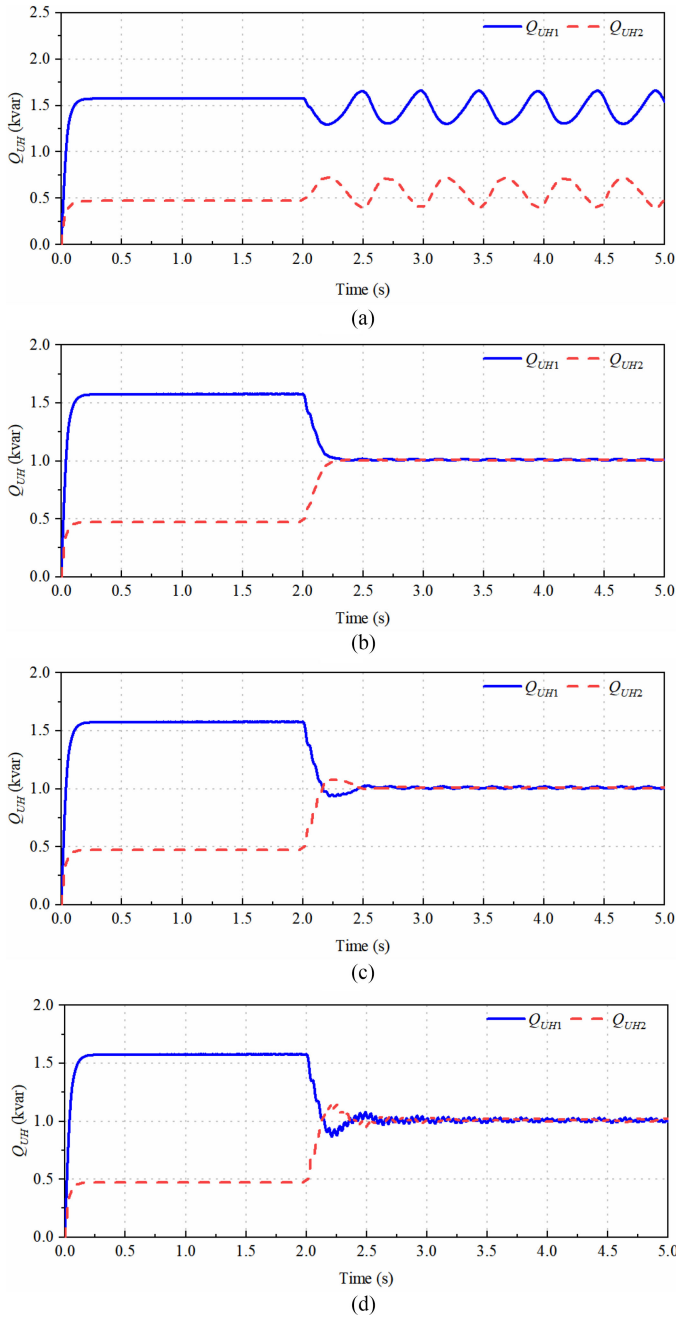
Fig. 17. Simulated waveforms of output unbalanced and harmonic power of DG1 and DG2 where the proposed control scheme is activated at 2.0 s under different coupling coefficient k_L. (a) $k_L = 0.002$. (b) $k_L = 0.004$. (c) $k_L = 0.005$. (d) $k_L = 0.006$.
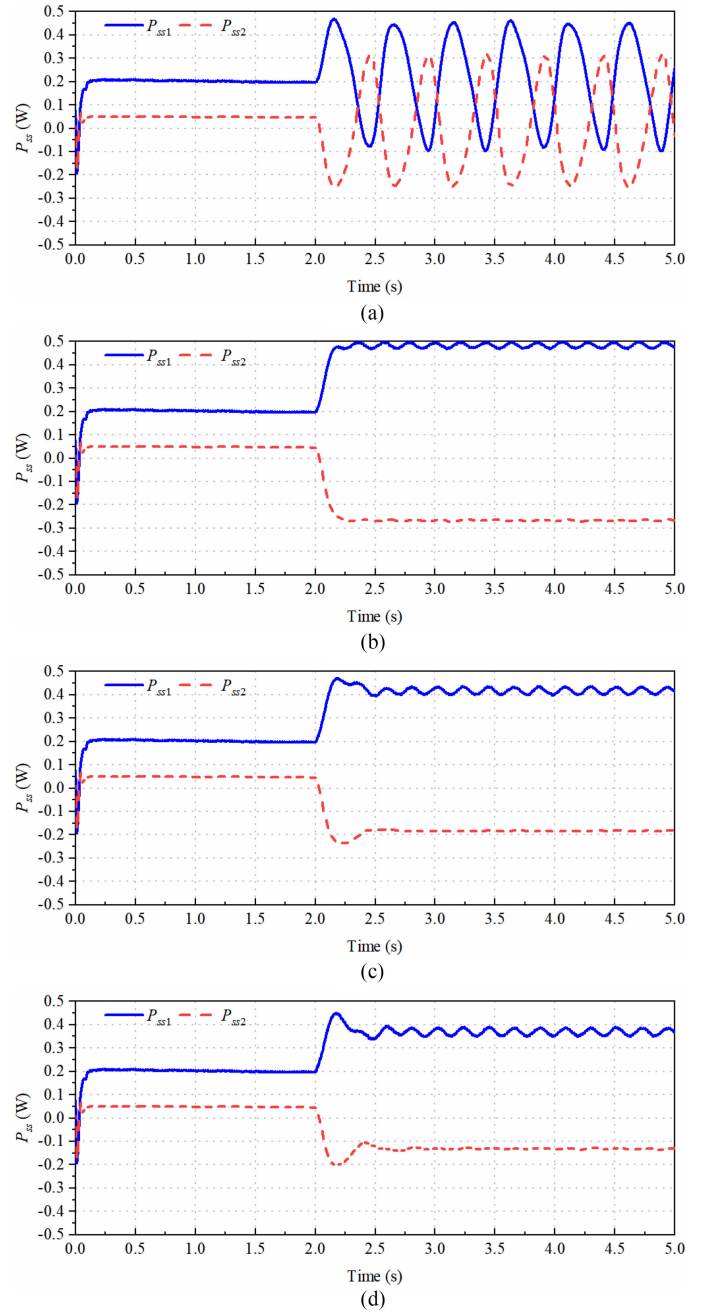

Fig. 18. Simulated waveforms of SACS active power of DG1 and DG2 where the proposed control scheme is activated at 2.0 s under different coupling coefficient k_L. (a) $k_L = 0.002$. (b) $k_L = 0.004$. (c) $k_L = 0.005$. (d) $k_L = 0.006$.

0.006, whereas unstable when k_L equals 0.002. This coincides with Criterion 1, where the power angle stability is not fulfilled if k_L is smaller than 0.0023 for the simulation case. The output SACS active power and virtual inductance for both DG units are shown in Figs. 18 and 19, respectively. These results indicate that as k_L increases, P_{ss1} decreases and P_{ss2} increases if the system is stable. The virtual inductance increases with the increase of k_L. Hence, (39) and (40) are proven.

Moreover, the THD in PCC voltage under different k_L values is demonstrated in Fig. 20. Note that there exists low-frequency fluctuation when k_L equals 0.002. This is because the system is unstable in this case and the PCC voltage begins to oscillate. For the three stable cases, the THD is increased along with the increase of k_L, which proves the validity of Criterion 2. It can also be noticed that voltage THD is always below the grid code requirement (8%), since the amplitude of SACS is carefully selected and k_L is well designed.
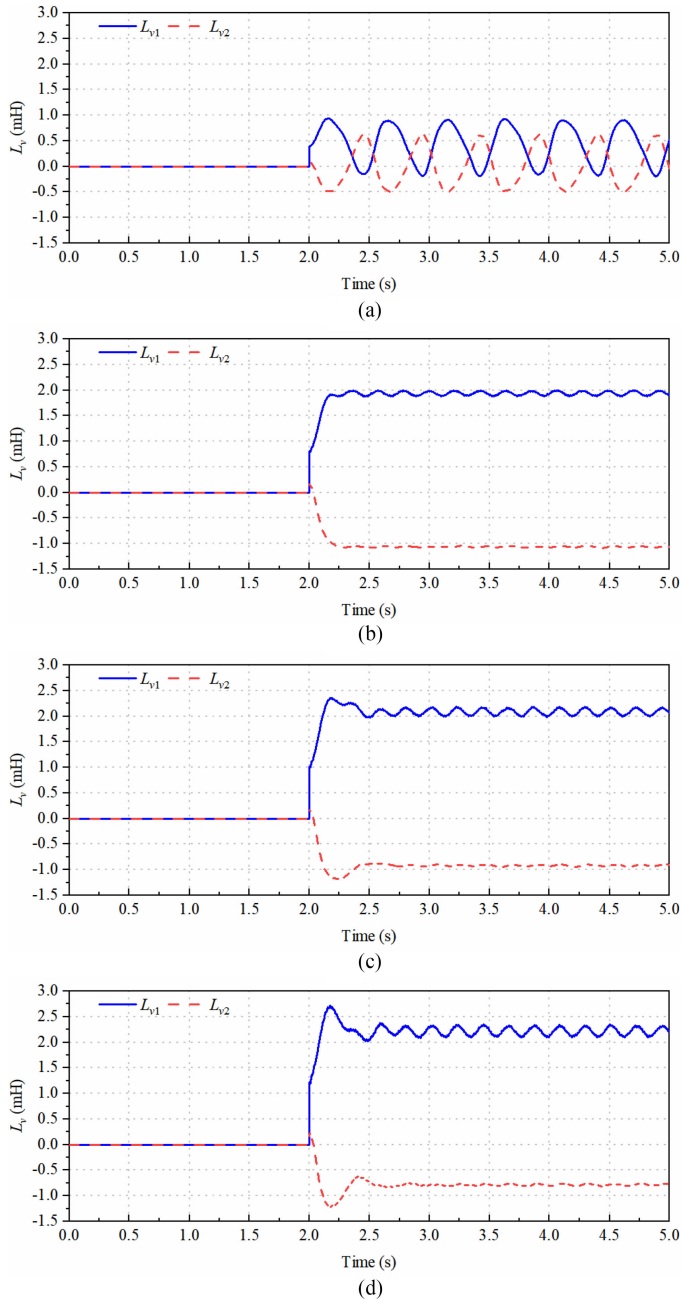
Fig. 19. Simulated waveforms of virtual inductance of DG1 and DG2 where the proposed control scheme is activated at 2.0 s under different coupling coefficient k_L. (a) $k_L = 0.002$. (b) $k_L = 0.004$. (c) $k_L = 0.005$. (d) $k_L = 0.006$.
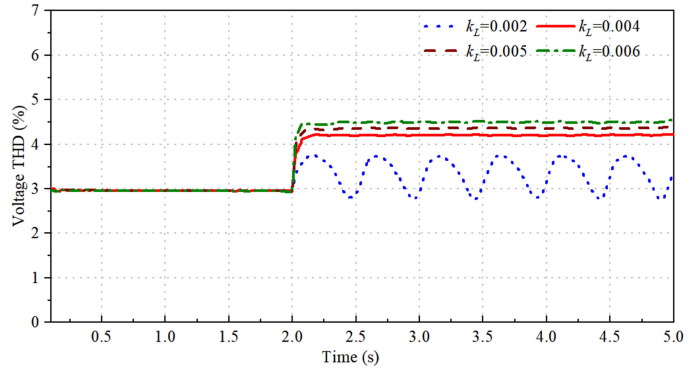

Fig. 20. Simulated waveforms of PCC voltage THD in the islanded microgrid where the proposed control scheme is activated at 2.0 s under different coupling coefficient k_L.
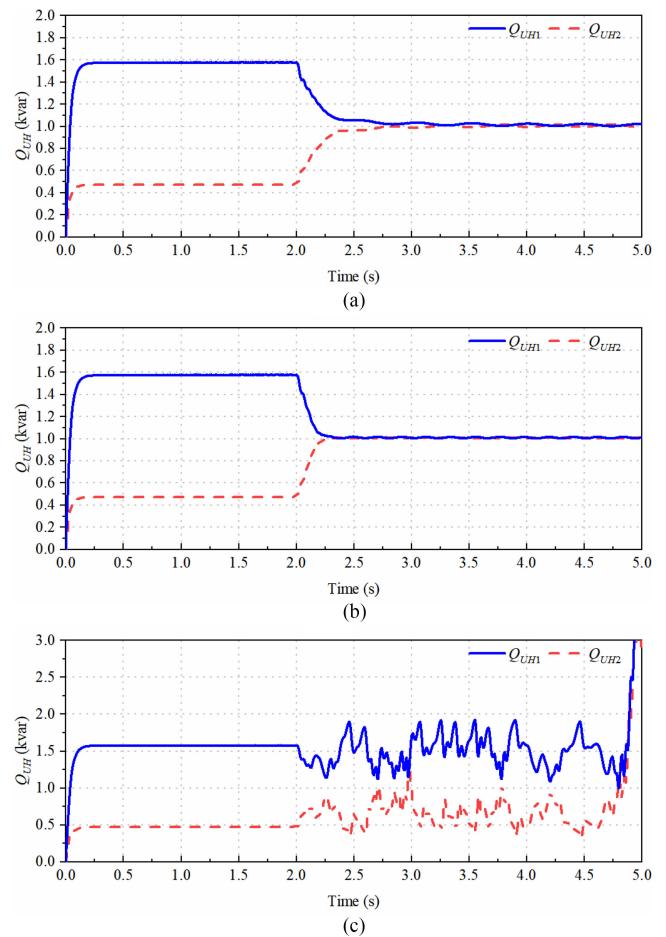

Fig. 21. Simulated waveforms of output unbalanced and harmonic power of DG1 and DG2 where the proposed control scheme is activated at 2.0 s under different droop coefficient k_{ss}. (a) $k_{ss} = 0.0063$. (b) $k_{ss} = 0.015$. (c) $k_{ss} = 0.15$.

3) k_{ss} Design Methodology Verification: Similarly, the effect of the droop coefficient can be studied by setting k_{ss} to 0.0063, 0.015, and 0.15, while k_L remains 0.004. According to (57), the maximum value of k_{ss} for the simulation case is 0.108. The waveform of Q_{UH} is shown in Fig. 21. As predicted by the small-signal perturbation model, the system dynamic response when k_{ss} equals 0.015 is faster than that when k_{ss} is set to 0.0063. However, the system becomes unstable when k_{ss} is designed to 0.15. Therefore, Criterion 3 is verified.

B. Experimental Results

To verify the effectiveness of the proposed power sharing method, the experimental results are provided based on a microgrid prototype as shown in Fig. 22. The experiment platform
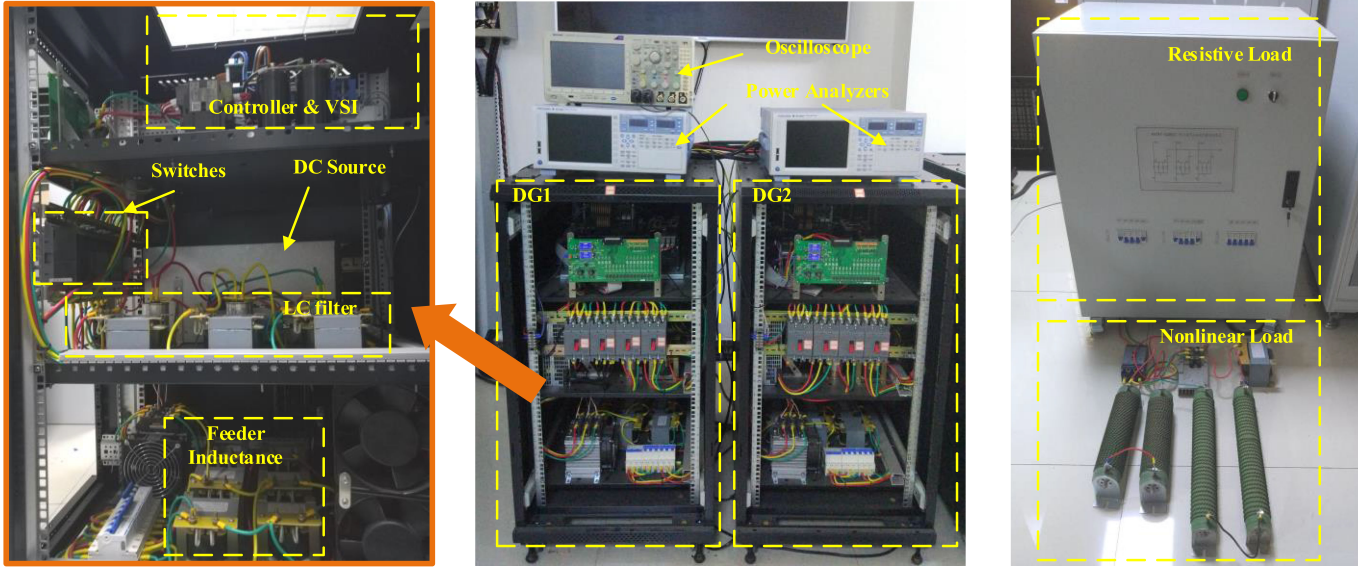
Fig. 22. Photograph of the experimental setup of islanded microgrid.

mainly consists of two three-leg three-phase 9-kVA inverters with *LC* filters in the same topology as shown in Fig. 1. Detailed power stage and control parameters are listed in Table I. The control algorithm is realized through DSP TMS320F28335 from Texas Instruments. Two power analyzers (YOKOGAWA WT1804E) are used to measure the output power, voltage, and current, and perform the harmonic analysis. The waveforms of active power, reactive power, and apparent power are drawn by Origin based on the data recorded by the power analyzer. The unbalanced and harmonic power is calculated in the DSP and displayed in the oscilloscope through DA converter.

To verify the power sharing effect comprehensively, two cases are conducted. In Case 1, the DG units are assumed to have same power ratings, so the load power should be equally shared by them. For Case 2, the power rating of DG1 is assumed to be half of DG2. So, the power should be shared in the ratio of 1:2. For both cases, the control algorithm consists of three steps. First, only traditional droop control is implemented before t_1. During t_1 to t_2, the unbalanced and harmonic power sharing method similar to that in [29]–[31] is demonstrated, and a direct droop between Q_{UH} and L_v is implemented as

$$L_v = L_{v0} - k_{dd}(Q_{UH0} - Q_{UH}) \qquad (58)$$

where k_{dd} is the droop coefficient designed by following the methodology in [29]–[31]. As mentioned in Section I, this kind of method cannot eliminate the unbalanced and harmonic power sharing error when the feeder impedance differs greatly. The purpose of employing this method is to highlight the effectiveness of the proposed method in a comparative way. Finally, the proposed power sharing method is activated after t_2.

1) Case 1: Equal Power Sharing: In this case, two DG units are assumed to have identical power rating, and the line inductances are about 1.2 and 2.8 mH, respectively. The output
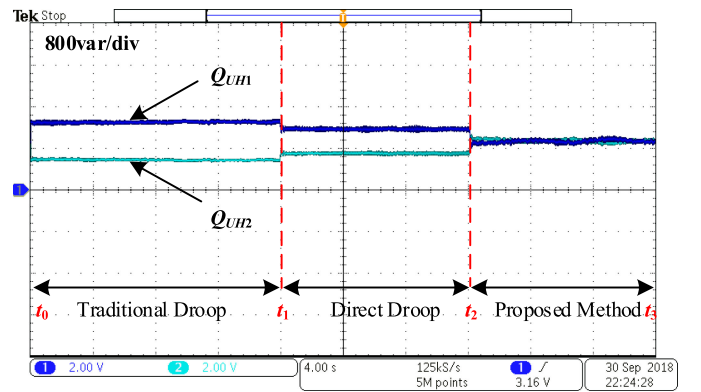

Fig. 23. Experimental waveforms of output unbalanced and harmonic power of DG1 and DG2 under the traditional droop method, the direct droop method, and the proposed control method.

unbalanced and harmonic powers of DG1 and DG2 are demonstrated in Fig. 23. The distributions of Q_{UH} are determined by the ratio of line inductance when traditional droop control is implemented between t_0 and t_1. Afterward, the power sharing performance is improved when the direct droop method as shown in (58) is activated at t_1. However, there still exists obvious power sharing error due to the limitations of the direct droop control method. After t_2, the proposed adaptive virtual impedance control method is implemented and the power sharing error is completely compensated and Q_{UH} is accurately shared by each DG unit. Moreover, the output apparent power, active power, and reactive power during the same process are shown in Fig. 24. It can be seen that the apparent power sharing performance is greatly improved after t_2 due to the equal sharing of unbalanced and harmonic power. Incidentally, the active power and reactive power waveforms remain almost
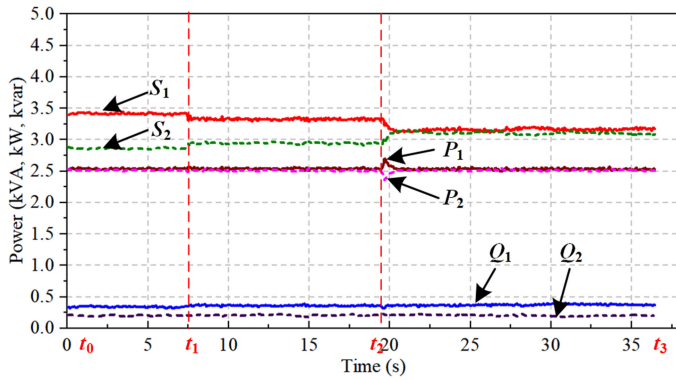
Fig. 24. Experimental waveforms of output apparent power, active power, and reactive power of DG1 and DG2 under the traditional droop method, the direct droop method, and the proposed control method.

unchanged during this whole process, meaning that the power sharing performance of $P–\omega$ and $Q–E$ droop control is not affected by the proposed method. It should be noted that the slight fluctuations in active power and reactive power at t_2 result from the switch of control algorithm, which can be avoided if the proposed method is activated from the beginning.

The power sharing performance can also be demonstrated by comparing the output current waveform of each DG unit. The output currents of phases A and C under different control methods are shown in Fig. 25. It can be seen that the output currents of DG1 and DG2 differ greatly when the traditional droop control is implemented. The direct droop method improves the power sharing at some degree, but the current sharing error can still be observed. After implementing the proposed control method, an enhanced power sharing performance is shown in Fig. 25(c), where DG1 current and DG2 current are almost the same.

Fig. 26 shows the fast Fourier transform (FFT) analysis result of the PCC voltage under different control methods. All the harmonic components below 20th order are demonstrated. It can be noticed that both the THD and each order harmonic component for the three studied control methods can satisfy the grid code. The THD under the proposed method is higher than that under the traditional droop method, but is lower than that under the direct droop method. Moreover, the increase of fourth harmonic voltage can be clearly observed. This is because the SACS is injected at 200 Hz with an amplitude about 1% of the fundamental voltage. Due to the good design of SACS amplitude and k_L, the total distortion percentage of the proposed method is below the grid code limitation.

2) Case 2: Proportional Power Sharing: In this case study, the power rating of DG1 is assumed to be half of DG2. The line inductance is designed to be identical for both DG units (about 2.8 mH). To realize the proportional power sharing according to the rating of DG inverter, the droop coefficients for $P–\omega$ droop, $Q–E$ droop, and the proposed $Q_{UH}–\omega_{ss}$ droop are designed based on (8), (9), and (20) as listed in Table I.

Following the same procedure as the previous case, the corresponding power waveform, current waveform, and THD results of the PCC voltage are shown in Figs. 27–30, respectively. From Fig. 27, it can be seen that Q_{UH1} and Q_{UH2} are almost
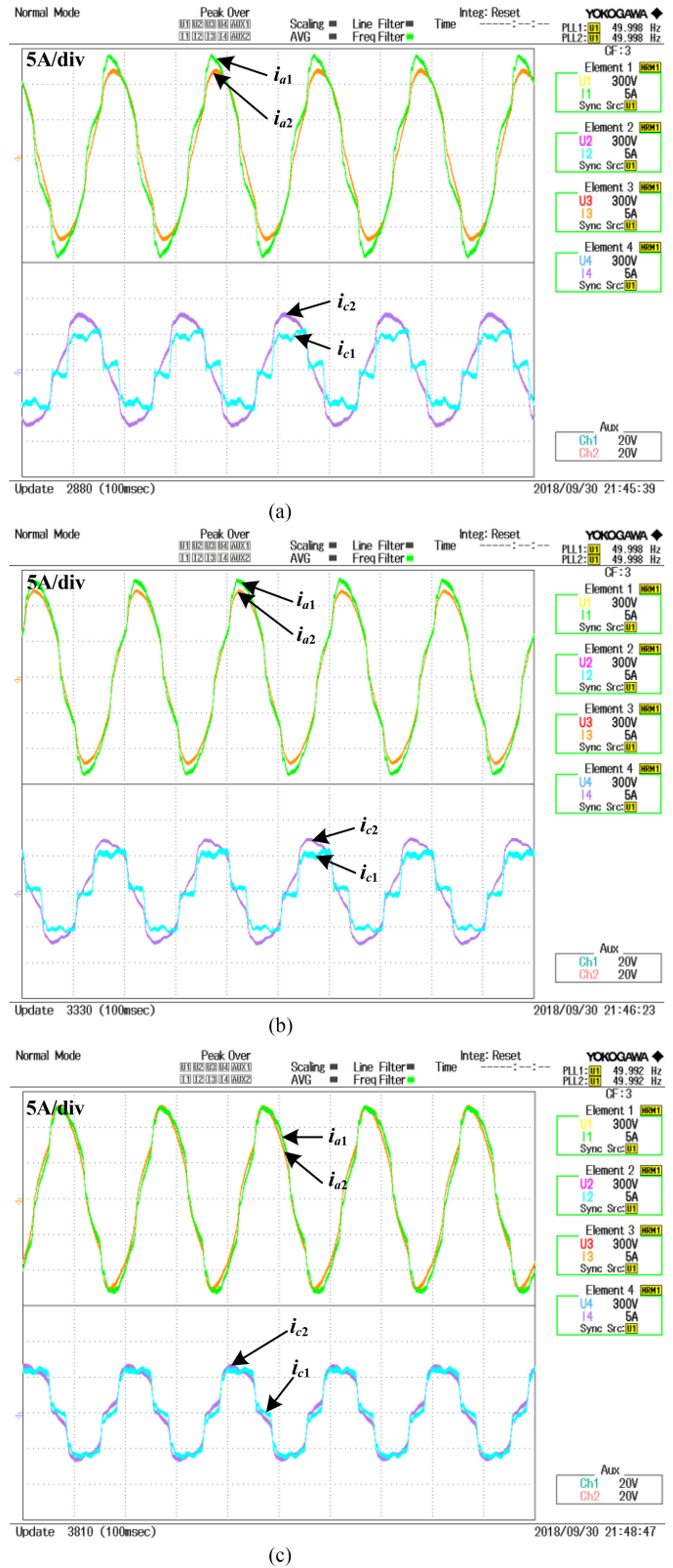

(a)

(b)

(c)

Fig. 25. Experimental waveforms of output current in phases A and C of DG1 and DG2 under (a) the traditional droop method, where $I_{a1} = 9.47$ A, $I_{a2} = 8.54$ A, $I_{c1} = 3.94$ A, and $I_{c2} = 5.65$ A; (b) the direct droop method, where $I_{a1} = 9.34$ A, $I_{a2} = 8.68$ A, $I_{c1} = 4.22$ A, and $I_{c2} = 5.28$ A; and (c) the proposed control method, where $I_{a1} = 8.98$ A, $I_{a2} = 9.09$ A, $I_{c1} = 4.81$ A, $I_{c2} = 4.81$ A.
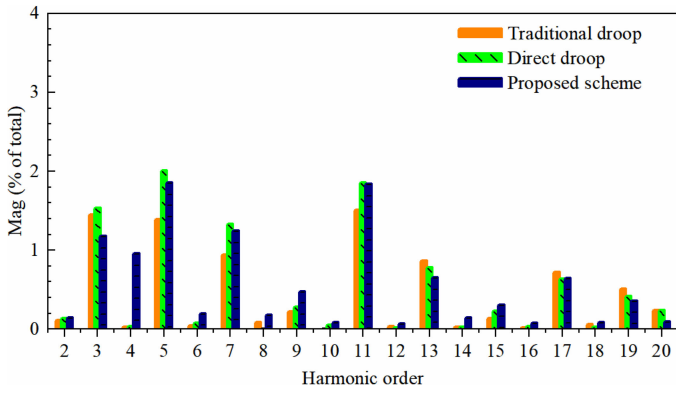
Fig. 26. FFT analysis results of the PCC voltage for the experimental islanded microgrid under the traditional droop method, the direct droop method, and the proposed control method, while the measured THD values of PCC voltage under these three cases are 3.417%, 4.537%, and 4.048%, respectively.
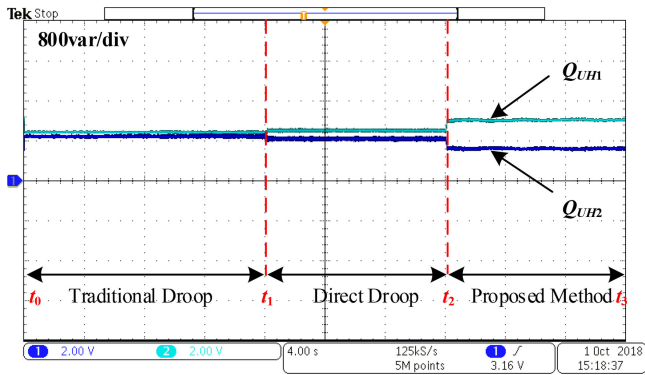

Fig. 27. Experimental waveforms of output unbalanced and harmonic power of DG1 and DG2 under the traditional droop method, the direct droop method, and the proposed control method when the power rating of DG1 is half of DG2.
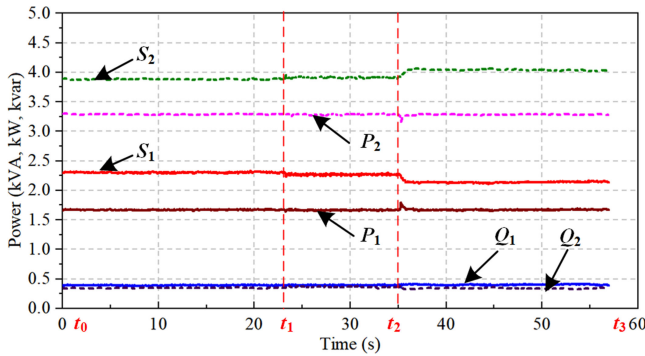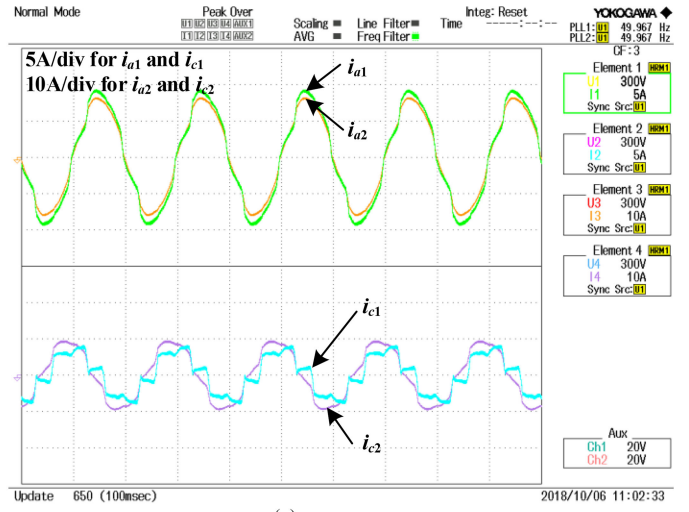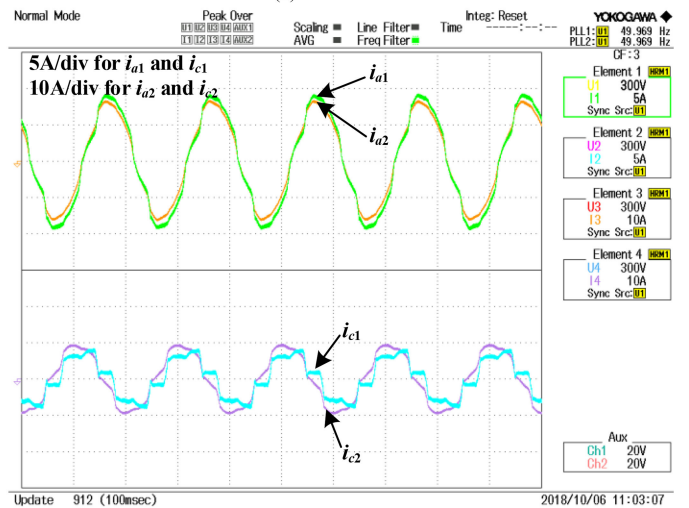

Fig. 28. Experimental waveforms of output apparent power, active power, and reactive power of DG1 and DG2 under the traditional droop method, the direct droop method, and the proposed control method when the power rating of DG1 is half of DG2.

same under traditional droop control, because the line inductance is same for both DG units in this case. Afterward, the direct droop method improves the power proportional sharing performance, but the sharing ratio is not 1:2. When the proposed control method is applied, the unbalanced and harmonic

Fig. 29. Experimental waveforms of output current in phases A and C of DG1 and DG2 under (a) the traditional droop method, where $I_{a1} = 6.32$ A, $I_{a2} = 11.44$ A, $I_{c1} = 2.54$ A, and $I_{c2} = 6.92$ A; (b) the direct droop method, where $I_{a1} = 6.30$ A, $I_{a2} = 11.52$ A, $I_{c1} = 2.65$ A, and $I_{c2} = 6.75$ A; and (c) the proposed control method, where $I_{a1} = 5.98$ A, $I_{a2} = 11.82$ A, $I_{c1} = 3.17$ A, and $I_{c2} = 6.26$ A, when the power rating of DG1 is half of DG2.

Fig. 30. FFT analysis results of the PCC voltage for the experimental islanded microgrid under the traditional droop method, the direct droop method, and the proposed control method when the power rating of DG1 is half of DG2, while the measured THD values of PCC voltage under these three case are 4.782%, 4.947%, and 4.873%, respectively.
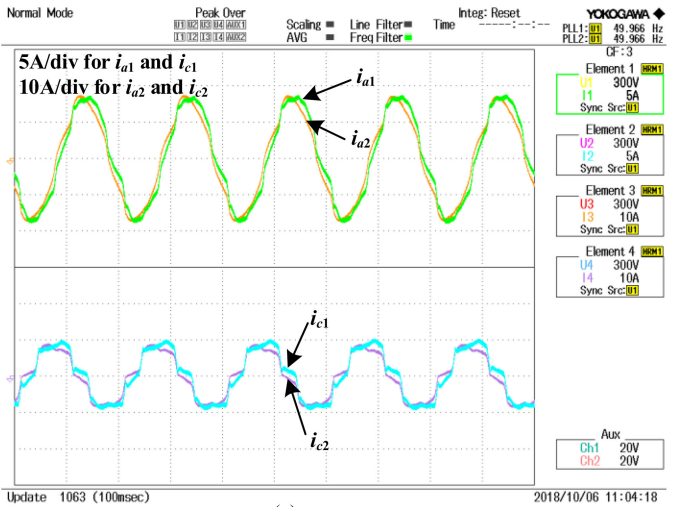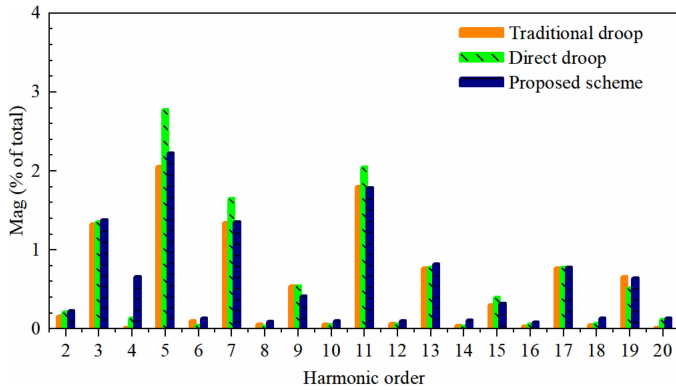
power is accurately shared by DG1 and DG2 according to their power ratings. According to Fig. 28, even when the proposed control method is not activated, the active power can be shared by DG1 and DG2 in the ratio of 1:2 due to $P–\omega$ droop. However, the apparent power is not accurately shared in the ratio of 1:2 until the proposed control method is applied and Q_{UH} is proportionally shared.

The output currents of DG1 and DG2 under different control methods are shown in Fig. 29. Note that the scale of the vertical axis is 5 A/div for DG1 and 10 A/div for DG2 to highlight the proportional power sharing performance. It can be seen that the current profiles for DG1 and DG2 differ greatly when traditional droop control or direct droop control is applied. However, the profiles of DG1 current and DG2 current are similar when the proposed method is implemented. In addition, the THD results of the PCC voltage under three different control methods are shown in Fig. 30, and similar conclusions as the previous case can be obtained.

VI. CONCLUSION

This paper proposes an adaptive virtual impedance control scheme for unbalanced and harmonic power sharing in islanded microgrids, based on the assistance of an extra small ac signal. In addition to the traditional $P–\omega$ and $Q–E$ droop, the proposed method utilizes $Q_{UH}–\omega_{ss}$ and $P_{ss}–L_v$ droop to adaptively regulate the virtual impedance for accurately sharing unbalanced and harmonic power. Moreover, the stability analysis and parameter design methodology are provided for the proposed method. Compared with the existing methods, the proposed scheme can completely compensate the power sharing error without communication link, and the plug-and-play feature is ensured. Meanwhile, there is no requirement on the knowledge of feeder impedances in advance in the proposed scheme. Furthermore, the voltage control loop is not varied with the active power of SACS, and the dynamic performance and system stability is less impacted by unbalanced and harmonics power

sharing. Note that the feeder impedance is assumed to be inductive to simplify the analysis. The same conclusions can be drawn when the feeder impedance is resistive, as long as replacing the virtual inductance L_v with a virtual resistance R_v. As for the cases when the feeder impedance combines inductance and resistance, the proposed method can only ensure the sharing of Q_{UH} and rms value of current. However, the sharing of each order harmonic current may not be accurate. The effectiveness of the proposed control method is validated by simulation and experimental results.

REFERENCES

[1] F. Blaabjerg, R. Teodorescu, M. Liserre, and A. V. Timbus, "Overview of control and grid synchronization for distributed power generation systems," *IEEE Trans. Ind. Electron.*, vol. 53, no. 5, pp. 1398–1409, Oct. 2006.

[2] S. Parhizi, H. Lotfi, A. Khodaei, and S. Bahramirad, "State of the art in research on microgrids: A review," *IEEE Access*, vol. 3, pp. 890–925, Jun. 2015.

[3] F. Blaabjerg, C. Zhe, and S. B. Kjaer, "Power electronics as efficient interface in dispersed power generation systems," *IEEE Trans. Power Electron.*, vol. 19, no. 5, pp. 1184–1194, Sep. 2004.

[4] M. C. Chandorkar, D. M. Divan, and R. Adapa, "Control of parallel connected inverters in standalone AC supply systems," *IEEE Trans. Ind. Appl.*, vol. 29, no. 1, pp. 136–143, Jan. 1993.

[5] J. M. Guerrero, L. Hang, and J. Uceda, "Control of distributed uninterruptible power supply systems," *IEEE Trans. Ind. Electron.*, vol. 55, no. 8, pp. 2845–2859, Aug. 2008.

[6] J. Rocabert, A. Luna, F. Blaabjerg, and P. Rodríguez, "Control of power converters in AC microgrids," *IEEE Trans. Power Electron.*, vol. 27, no. 11, pp. 4734–4749, Nov. 2012.

[7] W. Yao, M. Chen, J. Matas, J. M. Guerrero, and Z. M. Qian, "Design and analysis of the droop control method for parallel inverters considering the impact of the complex impedance on the power sharing," *IEEE Trans. Ind. Electron.*, vol. 58, no. 2, pp. 576–588, Feb. 2011.

[8] P. Rodríguez, A. V. Timbus, R. Teodorescu, M. Liserre, and F. Blaabjerg, "Flexible active power control of distributed power generation systems during grid faults," *IEEE Trans. Ind. Electron.*, vol. 54, no. 5, pp. 2583–2592, Oct. 2007.

[9] J. He, Y. W. Li, F. Blaabjerg, and X. Wang, "Active harmonic filtering using current-controlled, grid-connected DG units with closed-loop power control," *IEEE Trans. Power Electron.*, vol. 29, no. 2, pp. 642–653, Feb. 2014.

[10] J. He and Y. W. Li, "An enhanced microgrid load demand sharing strategy," *IEEE Trans. Power Electron.*, vol. 27, no. 9, pp. 3984–3995, Sep. 2012.

[11] H. Han, Y. Liu, Y. Sun, M. Su, and J. M. Guerrero, "An improved droop control strategy for reactive power sharing in islanded microgrid," *IEEE Trans. Power Electron.*, vol. 30, no. 6, pp. 3133–3141, Jun. 2015.

[12] Q. C. Zhong, Y. Wang, and B. Ren, "UDE-based robust droop control of inverters in parallel operation," *IEEE Trans. Ind. Electron.*, vol. 64, no. 9, pp. 7552–7562, Sep. 2017.

[13] Y. Zhu, F. Zhuo, F. Wang, B. Liu, and Y. Zhao, "A wireless load sharing strategy for islanded microgrid based on feeder current sensing," *IEEE Trans. Power Electron.*, vol. 30, no. 12, pp. 6706–6719, Dec. 2015.

[14] M. Savaghebi, A. Jalilian, J. C. Vasquez, and J. M. Guerrero, "Secondary control for voltage quality enhancement in microgrids," *IEEE Trans. Smart Grid*, vol. 3, no. 4, pp. 1893–1902, Dec. 2012.

[15] L. Meng, F. Tang, M. Savaghebi, J. C. Vasquez, and J. M. Guerrero, "Tertiary control of voltage unbalance compensation for optimal power quality in islanded microgrids," *IEEE Trans. Energy Convers.*, vol. 29, no. 4, pp. 802–815, Dec. 2014.

[16] F. Guo, C. Wen, J. Mao, J. Chen, and Y. D. Song, "Distributed cooperative secondary control for voltage unbalance compensation in an islanded microgrid," *IEEE Trans. Ind. Inform.*, vol. 11, no. 5, pp. 1078–1088, Oct. 2015.

[17] Y. Han, P. Shen, X. Zhao, and J. M. Guerrero, "An enhanced power sharing scheme for voltage unbalance and harmonics compensation in an islanded AC microgrid," *IEEE Trans. Energy Convers.*, vol. 31, no. 3, pp. 1037–1050, Sep. 2016.

[18] J. He, Y. W. Li, J. M. Guerrero, F. Blaabjerg, and J. C. Vasquez, "An island-ing microgrid power sharing approach using enhanced virtual impedance control scheme," *IEEE Trans. Power Electron.*, vol. 28, no. 11, pp. 5272–5282, Nov. 2013.

[19] J. He, Y. W. Li, and F. Blaabjerg, "An enhanced islanding microgrid reactive power, imbalance power, and harmonic power sharing scheme," *IEEE Trans. Power Electron.*, vol. 30, no. 6, pp. 3389–3401, Jun. 2015.

[20] H. Moussa, A. Shahin, J. P. Martin, B. Nahid-Mobarakeh, S. Pierfederici, and N. Moubayed, "Harmonic power sharing with voltage distortion compensation of droop controlled islanded microgrids," *IEEE Trans. Smart Grid*, vol. 9, no. 5, pp. 5335–5347, Sep. 2018.

[21] L. Meng *et al.*, "Distributed voltage unbalance compensation in islanded microgrids by using a dynamic consensus algorithm," *IEEE Trans. Power Electron.*, vol. 31, no. 1, pp. 827–838, Jan. 2016.

[22] J. Zhou, S. Kim, H. Zhang, Q. Sun, and R. Han, "Consensus-based distributed control for accurate reactive, harmonic, and imbalance power sharing in microgrids," *IEEE Trans. Smart Grid*, vol. 9, no. 4, pp. 2453–2467, Jul. 2018.

[23] V. C. Gungor *et al.*, "Smart grid technologies: communication technologies and standards," *IEEE Trans. Ind. Inform.*, vol. 7, no. 4, pp. 529–539, Nov. 2011.

[24] U. Borup, F. Blaabjerg, and P. N. Enjeti, "Sharing of nonlinear load in parallel-connected three-phase converters," *IEEE Trans. Ind. Appl.*, vol. 37, no. 6, pp. 1817–1823, Nov. 2001.

[25] J. M. Guerrero, J. Matas, L. G. D. Vicuña, M. Castilla, and J. Miret, "Wireless-control strategy for parallel operation of distributed-generation inverters," *IEEE Trans. Ind. Electron.*, vol. 53, no. 5, pp. 1461–1470, Oct. 2006.

[26] D. De and V. Ramanarayanan, "Decentralized parallel operation of inverters sharing unbalanced and nonlinear loads," *IEEE Trans. Power Electron.*, vol. 25, no. 12, pp. 3015–3025, Dec. 2010.

[27] T. Vandoorn, B. Meersman, J. D. Kooning, and L. Vandevelde, "Controllable harmonic current sharing in islanded microgrids: DG units with programmable resistive behavior toward harmonics," *IEEE Trans. Power Del.*, vol. 27, no. 2, pp. 831–841, Apr. 2012.

[28] X. Zhou, F. Tang, P. C. Loh, X. Jin, and W. Cao, "Four-leg converters with improved common current sharing and selective voltage-quality enhancement for islanded microgrids," *IEEE Trans. Power Del.*, vol. 31, no. 2, pp. 522–531, Apr. 2016.

[29] P. T. Cheng and T. L. Lee, "Distributed active filter systems (DAFSs): A new approach to power system harmonics," *IEEE Trans. Ind. Appl.*, vol. 42, no. 5, pp. 1301–1309, Sep. 2006.

[30] T. L. Lee and P. T. Cheng, "Design of a new cooperative harmonic filtering strategy for distributed generation interface converters in an islanding network," *IEEE Trans. Power Electron.*, vol. 22, no. 5, pp. 1919–1927, Sep. 2007.

[31] P. T. Cheng, C. A. Chen, T. L. Lee, and S. Y. Kuo, "A cooperative imbalance compensation method for distributed-generation interface converters," *IEEE Trans. Ind. Appl.*, vol. 45, no. 2, pp. 805–815, Mar. 2009.

[32] P. Sreekumar and V. Khadkikar, "A new virtual harmonic impedance scheme for harmonic power sharing in an islanded microgrid," *IEEE Trans. Power Del.*, vol. 31, no. 3, pp. 936–945, Jun. 2016.

[33] P. Sreekumar and V. Khadkikar, "Direct control of the inverter impedance to achieve controllable harmonic sharing in the islanded microgrid," *IEEE Trans. Ind. Electron.*, vol. 64, no. 1, pp. 827–837, Jan. 2017.

[34] A. Tuladhar, H. Jin, T. Unger, and K. Mauch, "Control of parallel inverters in distributed AC power systems with consideration of line impedance effect," *IEEE Trans. Ind. Appl.*, vol. 36, no. 1, pp. 131–138, Jan. 2000.

[35] *IEEE Standard Definitions for the Measurement of Electric Power Quantities Under Sinusoidal, Nonsinusoidal, Balanced, or Unbalanced Conditions*, IEEE Standard 1459-2010, 2010.

[36] *IEEE Recommended Practice and Requirements for Harmonic Control in Electric Power Systems*, IEEE Standard 519-2014 (revision of IEEE Standard 519-1992), 2014.

[37] M. Savaghebi, A. Jalilian, J. C. Vasquez, and J. M. Guerrero, "Secondary control for voltage quality enhancement in microgrids," *IEEE Trans. Smart Grid*, vol. 3, no. 4, pp. 1893–1902, Dec. 2012.

[38] J. M. Guerrero, J. Matas, L. Garcia de Vicuna, M. Castilla, and J. Miret, "Decentralized control for parallel operation of distributed generation inverters using resistive output impedance," *IEEE Trans. Ind. Electron.*, vol. 54, no. 2, pp. 994–1004, Apr. 2007.

[39] J. He and Y. W. Li, "Analysis, design, and implementation of virtual impedance for power electronics interfaced distributed generation," *IEEE Trans. Ind. Appl.*, vol. 47, no. 6, pp. 2525–2538, Nov. 2011.

[40] *IEEE Recommended Practice and Requirements for Harmonic Control in Electric Power Systems*, IEEE Standard 519-2014 (revision of IEEE Standard 519-1992), 2014.

[41] P. Rodriguez, A. Luna, I. Candela, R. Mujal, R. Teodorescu, and F. Blaabjerg, "Multiresonant frequency-locked loop for grid synchronization of power converters under distorted grid conditions," *IEEE Trans. Ind. Electron.*, vol. 58, no. 1, pp. 127–138, Jan. 2011.

[42] E. A. A. Coelho, P. C. Cortizo, and P. F. D. Garcia, "Small-signal stability for parallel-connected inverters in stand-alone AC supply systems," *IEEE Trans. Ind. Appl.*, vol. 38, no. 2, pp. 533–542, Mar. 2002.

[43] N. Pogaku, M. Prodanovic, and T. C. Green, "Modeling, analysis, and testing of autonomous operation of an inverter-based microgrid," *IEEE Trans. Power Electron.*, vol. 22, no. 2, pp. 613–625, Mar. 2007.

[44] X. Wang, Y. W. Li, F. Blaabjerg, and P. C. Loh, "Virtual-impedance-based control for voltage-source and current-source converters," *IEEE Trans. Power Electron.*, vol. 30, no. 12, pp. 7019–7037, Dec. 2015.

[45] J. Svensson, M. Bongiorno, and A. Sannino, "Practical implementation of delayed signal cancellation method for phase-sequence separation," *IEEE Trans. Power Del.*, vol. 22, no. 1, pp. 18–26, Jan. 2007.

[46] M. Hamzeh, H. Karimi, and H. Mokhtari, "A new control strategy for a multi-bus MV microgrid under unbalanced conditions," *IEEE Trans. Power Syst.*, vol. 27, no. 4, pp. 2225–2232, Nov. 2012.

[47] P. Kundur, *Power System Stability and Control*. New York, NY, USA: McGraw-Hill, 1994.

[48] *Guide on Security and Stability for Power Systems*, Chinese Electric Power Industry Standard DL 755-2001, 2001.

Baojin Liu (S'15) received the B.S. degree in electrical engineering and automation from Dalian Maritime University, Dalian, China, in 2014, and is currently working toward the Ph.D. degree with Xi'an Jiaotong University (XJTU), Xi'an, China.

His research interests include coordinative control of parallel inverters and power quality control in ac microgrid.

Zeng Liu (S'09–M'14) received the B.S. degree in electrical engineering from Hunan University, Changsha, China, in 2006, and the M.S. and Ph.D. degrees in electrical engineering from XJTU, Xi'an, China, in 2009 and 2013, respectively.

He joined XJTU as a Faculty Member of electrical engineering, where he is currently an Associate Professor. From 2015 to 2017, he was a Visiting Scholar with the Center for Power Electronics Systems, Virginia Polytechnic Institute and State University, Blacksburg, VA, USA. His research interests include control of parallel inverters, transfer control of grid-tied inverters, and small-signal stability of three-phase ac power electronics systems.

Jinjun Liu (M'97–SM'10–F'19) received the B.S. and Ph.D. degrees in electrical engineering from XJTU, Xi'an, China, in 1992 and 1997, respectively.

He joined the Electrical Engineering School, XJTU, Xi'an, China, as a Faculty. From late 1999 to early 2002, he was a Visiting Scholar with the Center for Power Electronics Systems, Virginia Polytechnic Institute and State University, Blacksburg, VA, USA. In late 2002, he was promoted to a Full Professor and then the Head of the Power Electronics and Renewable Energy Center, XJTU, Xi'an, China, which now comprises 17 faculty members and over 100 graduate students and carries one of the leading power electronics programs in China. From 2005 to early 2010, he was an Associate Dean of Electrical Engineering School, XJTU, and from 2009 to early 2015, the Dean for Undergraduate Education of XJTU. He is currently an XJTU Distinguished Professor of power electronics, sponsored by Chang Jiang Scholars Program of Chinese Ministry of Education. He has coauthored three books (including one textbook), authored more than 400 technical papers in peer-reviewed journals and conference proceedings, holds nearly 50 invention patents (China and U.S.), and delivered for many times plenary keynote speeches and tutorials at IEEE conferences or China national conferences in power electronics area. His research interests include power quality control and utility applications of power electronics, microgrids for sustainable energy and distributed generation, and more/all electronic power systems.

Dr. Liu was the recipient of, for eight times, governmental awards at national level or provincial/ministerial level for scientific research/teaching achievements, the 2006 Delta Scholar Award, the 2014 Chang Jiang Scholar Award, the 2014 Outstanding Sci-Tech Worker of the Nation Award, and the IEEE Transactions on Power Electronics 2016 Prize Paper Award. He was the IEEE Power Electronics Society Region 10 Liaison and then China Liaison for ten years, an Associate Editor for the IEEE TRANSACTIONS ON POWER ELECTRONICS for 12 years, and starting from 2015, the Vice President for membership of IEEE PELS. He is on the Board of China Electrotechnical Society and was elected the Vice President of the CES Power Electronics Society in 2013. Since 2013, he is the Vice President for International Affairs, China Power Supply Society (CPSS), and the Vice Chair of the Chinese National Steering Committee for College Electric Power Engineering Programs, and since 2016, the inaugural Editor-in-Chief for *CPSS Transactions on Power Electronics and Applications*.

Ronghui An (S'18) received the B.S. degree in electrical engineering and automation in 2016 from XJTU, Xi'an, China, where he is currently working toward the Ph.D. degree.

His research interests include coordinated control and optimal design of distributed generation, and planning and designing of microgrid systems.

Haoyang Zheng received the B.S. degree in electrical engineering and automation in 2017 from XJTU, Xi'an, China, where he is currently working toward the Ph.D. degree.

His research interests include the control of parallel three-phase inverters for uninterrupted power supply and microgrid application, such as droop control and seamless transfer.

Yidong Shi received the B.S. degree in electrical engineering and automation from the Northwestern Polytechnical University, Xi'an, China, in 2018, and is currently working toward the M.S. degree with XJTU, Xi'an, China.

His research interests include the control of parallel three-phase inverters for uninterrupted power supply and microgrid application.